

REPORT DOCUMENTATION PAGE

OMB No. 0704-0188

Public reporting burden for this collection of information is estimated to average 1 hour per response, including the time for reviewing instructions, searching data sources, gathering and maintaining the data needed, and completing and reviewing the collection of information. Send comments regarding this burden estimate or any other aspect of this collection of information, including suggestions for reducing this burden to Washington Headquarters Service, Directorate for Information Operations and Reports, 1215 Jefferson Davis Highway, Suite 1204, Arlington, VA 22202-4302, and to the Office of Management and Budget, Paperwork Reduction Project (0704-0188) Washington, DC 20503.

PLEASE DO NOT RETURN YOUR FORM TO THE ABOVE ADDRESS.

1. REPORT DATE (DD-MM-YYYY) 30 Sept 2009		2. REPORT TYPE Final Technical Report		3. DATES COVERED (From – To) 1 Feb 2006-30 Nov 2008	
4. TITLE AND SUBTITLE Studies of Microdischarge Plasma Thrusters for Nanosatellite Propulsion				5a. CONTRACT NUMBER FA9550-06-1-0176	
				5b. GRANT NUMBER	
				5c. PROGRAM ELEMENT NUMBER	
6. AUTHOR(S) Laxminarayan L. Raja				5d. PROJECT NUMBER	
				5e. TASK NUMBER	
				5f. WORK UNIT NUMBER	
7. PERFORMING ORGANIZATION NAME(S) AND ADDRESS(ES) The University of Texas at Austin Austin, Texas 78712				8. PERFORMING ORGANIZATION REPORT NUMBER	
9. SPONSORING/MONITORING AGENCY NAME(S) AND ADDRESS(ES) USAF/AFRL AFOSR 875 North Randolph Street Arlington VA 22203				10. SPONSOR/MONITOR'S ACRONYM(S) AFOSR	
				11. SPONSORING/MONITORING AGENCY REPORT NUMBER N/A	
12. DISTRIBUTION AVAILABILITY STATEMENT Distribution Statement A: Approved for public release. Distribution is unlimited.					
13. SUPPLEMENTARY NOTES					
14. ABSTRACT <p>The objective of this project is the development and study of a new class of propulsion device call the Micro discharge Plasma Thruster (MPT). The MPT thruster is intended for small satellite propulsion and is expected to have several advantages over competing small satellite propulsion devices, such as cold gas micro thrusters, MEMS fabricated resist jets, microPPT, FEEP devices, and miniaturized version of Hall thrusters and Ion thrusters. The primary advantages of the MPT being operation with a variety of propellant gases (noble and molecular gases), very small dimensions, and low voltage (~ 100's V) direct-current operation. A number of diagnostics have been implemented including an ion beam probe, and emission spectroscopy to determine the physical and chemical state of the micro plasma and the plume from the MPT device. We have also identified and discussed the problem of erosion in the device. Details of the experimental are given in the next section. In the computational work we have made significant progress in developing an entire suite of tools to provide high-fidelity computations of the MPT thruster. A self-consistent, multi-species, multi-temperature model for the MPT discharge and a model for the low-Reynolds number, high-Mach number compressible flow through the MPT have been developed and coupled together.</p>					
15. SUBJECT TERMS					
16. SECURITY CLASSIFICATION OF:		17. LIMITATION OF ABSTRACT		18. NUMBER OF PAGES 11	
				19a. NAME OF RESPONSIBLE PERSON Standard Form 298 (Rev. 8-98) Prescribed by ANSI Std Z39-18	

FINAL PERFORMANCE REPORT

Performance period: Feb 01, 2006 – Nov 30, 2008

Project Title: Studies of Microdischarge Plasma Thrusters for Nanosatellite Propulsion

AFOSR Award no.: FA9550-06-1-0176

Project Start Date: Feb. 01, 2006

Project monitor: Dr. Mitat Birkan

Principal Investigator:

Laxminarayan L. Raja

Associate Professor

Dept. of Aerospace Engineering and Engineering Mechanics

The University of Texas at Austin

Austin, Texas 78712

Co-Principal Investigator:

Philip L. Varghese

Professor

Dept. of Aerospace Engineering and Engineering Mechanics

The University of Texas at Austin

Austin, Texas 78712

20130919085

Status of Effort:

The objective of this project is the development and study of a new class of propulsion device call the Microdischarge Plasma Thruster (MPT). The MPT thruster is intended for small satellite propulsion and is expected to have several advantages over competing small satellite propulsion devices, such as cold gas microthrusters, MEMS fabricated resistojets, microPPT, FEEP devices, and miniaturized version of Hall thrusters and Ion thrusters. The primary advantages of the MPT being operation with a variety of propellant gases (noble and molecular gases), very small dimensions, and low voltage (~ 100 's V) direct-current operation.

The 3-year effort discussed in this report is broadly divided into an experimental component and a computational modeling component. We have achieved a reasonable degree of success with both components of our research during this project.

As will be discussed in the experimental section, this project has enabled us to conclusively demonstrate that it is possible to establish a stable and self-sustained microdischarge plasma in a gas propellant flow-through situation with gas efflux into vacuum. A number of diagnostics have been implemented including an ion beam probe, and emission spectroscopy to determine the physical and chemical state of the microplasma and the plume from the MPT device. We have also identified and discussed the problem of erosion in the device. Details of the experimental are given in the next section.

In the computational work we have made significant progress in developing an entire suite of tools to provide high-fidelity computations of the MPT thruster. A self-consistent, multi-species, multi-temperature model for the MPT discharge and a model for the low-Reynolds number, high-Mach number compressible flow through the MPT have been developed and coupled together. The models have been exercised to provide a detailed understanding of the MPT propulsion device operation. Details are provided in the next section.

Accomplishments and New Findings:

Experimental Investigation of Micro Plasma Thruster (MPT)

I. Introduction

In comparison to large satellites, small satellites are more suitable choice for formation flying and multivehicle operations [1]. Because of small size and mass, they are also relatively easier to test and assemble. Such satellites typically weigh less than 100 kg. In this category, nanosatellites weigh ~ 10 kg and have linear dimensions of less than 50 cm. Their thrust requirements range from $\sim 1 \mu\text{N}$ for small impulse bit precision applications to ~ 10 mN for satellite slew maneuvers. The construction of nanosatellite entails miniaturizing its components like the power source, electronics, navigation system, propulsion system, etc. However, a scaled down version of a large power source, electronics or a propulsion system is not always viable, and so alternative approaches must be explored to invent smaller systems.

There is significant ongoing research in the space propulsion community to develop micropropulsion devices, but options for nanosatellites are still very limited. Among the electric thrusters, the miniature hall thruster [2], [3], ion thruster [4], [5] and micro pulsed power thruster (microPPT) [6] are some examples of scaled down versions of large thrusters. The miniaturized hall thruster and ion thruster require operating power of ~ 100 W, which is in excess of what can be accommodated in a nanosatellite system where bus powers are less than 10-50 W. In contrast to this, the micro pulsed power thrusters (microPPT) can operate at ~ 10 W, but a peak pulse voltage can be several kV which imposes severe constraints on reducing the size of the power processing unit (PPU). Thrusters that are specifically geared towards micro propulsion also suffer from high voltage requirement. For example, the field emission electric propulsion (FEEP) thruster has high specific impulse ($\sim 10,000$ s) and it can generate thrust levels of ($10 \mu\text{N}$), but the input voltage is ~ 10 kV [7]. An additional drawback of the FEEP thruster is that it uses a liquid metal propellant like the liquid Cesium, which can pose contamination hazard. Colloid thruster is also similar to FEEP thruster [8]. Its performance characteristics are comparable to that of the FEEP thruster; specific impulse is ~ 1000 s and thrust level is $\sim 100 \mu\text{N}$, but it also has high voltage requirements. In this way, although some electric micro thruster devices have been proposed they do not provide complete solution for nanosatellite propulsion, mainly because of their high operating voltage and power.

Small scale versions of cold gas thrusters [9], resistojets [10] and combustion based thrusters [11] are also not desirable for nanosatellite propulsion. In combustion based micron-scale devices it is difficult to stabilize combustion and store reactive propellant. The issues related with preheating and lifetime of catalysts can also complicate combustion in a micron-scale devices. The miniaturized cold gas thrusters and resistojets have low specific impulse (~ 100 s or less), which is also not ideal for micropropulsion.

High specific impulse can possibly be attained in a scaled down version of plasma based arcjet thruster, but miniaturization of such a thruster is limited by plasma quenching and required conditions for plasma breakdown. As predicted by Paschen curves [12], the minimum value of breakdown voltage for most gases is ~ 100 V, and at the minimum break down voltage, pd , which is the product of pressure (p) and inter electrode distance (d), is ~ 10 Torr-cm. The breakdown voltage increases sharply for higher or lower pd values. As the discharge dimension or d decreases the required break down voltage can become extremely high. Also, when the size of the propulsion device is decreased the ratio of its surface area to volume increases. For a given volume of plasma, this provides larger area for charged species to recombine, and so the quenching phenomenon hinders plasma ignition and stabilization in a micron-scale device.

The MPT overcomes plasma quenching and high voltage requirements. Unlike an arc jet thruster, it is based on a direct current micro discharge. The micro hall thruster (MHT) [13] also utilizes a direct current

micro-discharge, but it requires an external magnetic field to stabilize the plasma. The plasma in an MPT is self sustaining and so an external magnetic field is not necessary.

As shown in Fig. 1, the MPT has a multilayer sandwich structure. It has three electrodes- e_1 , e_2 , e_3 which are $\sim 100 \mu\text{m}$ thick and they are separated by $\sim 200 \mu\text{m}$ thick dielectrics- m_1 , m_2 and m_3 . As illustrated in Fig. 1 it has a narrow duct $\sim 100 \mu\text{m}$ in diameter which expands to $\sim 330 \mu\text{m}$ downstream of the throat. From gas dynamic point of view the cavity inside the MPT resembles a converging diverging nozzle that can accelerate the gas to super sonic velocities downstream of the throat.

The operating mechanism of the MPT is as follows. The discharge is generated between e_1 and e_3 . It heats the neutral gas which accelerates as it flows in the converging diverging nozzle. The ion flow is also accelerated by the nozzle and the floating potential that exists between the MPT and the vacuum. The expulsion of hot gas and ions into the vacuum generates thrust. So far the MPT has been operated using argon. When the argon flow rate is 5 sccm, the pressure in the cavity ranges from ~ 100 Torr upstream to ~ 1 Torr near the exit. Between e_2 and e_3 , because the number density of gas species (N) is low, the ratio of characteristic electric field strength (E) to the number density of neutral species E/N is high. This is favorable to enhance ionization process in the discharge. Ordinarily, at pressures as low as ~ 1 Torr and linear dimensions of the order of few hundred microns, the break down voltage is in the order of several kV if the discharge is to be sustained only by secondary electron emissions at the cathode. The structure of the MPT helps to overcome such high voltage requirement to sustain the discharge. The high pressure (~ 100 Torr) between e_1 and e_2 helps to bring down the break down voltage of gas inside the MPT. The region of the discharge between e_1 and e_2 can also supply electrons to the region between e_2 and e_3 to increase and sustain ionization process in that region. In this way, MPT can be stably operated using a non corrosive/ non contaminating propellant at relatively low voltages.

II. Experimental Set Up

The MPT was operated inside a vacuum chamber. Experiments were carried out to determine the stable operating conditions, electrical characteristics of MPT and properties of the plume. The following section describes the apparatus and experimental set ups.

A. Vacuum System

The MPT is operated in a non-magnetic stainless steel vacuum chamber which is 0.15 m in diameter. The chamber consists of six symmetrically placed extensions of length 0.08 m and diameter 0.1 m, which provide access to the interior of the chamber. Optical access is provided by the glass viewports on the extensions. The glass is 4 mm thick and of type kodial, which means high frequencies like UV are absorbed by these viewports. The chamber is evacuated using a Varian TV-551 turbo molecular pump backed by Alcatel 2015 SD general vane roughing pump. Without gas flow, when the roughing pump evacuates to 15 mTorr, the turbo molecular pump is switched on to lower the chamber pressure to $\sim 1 \mu\text{Torr}$. When the pressure in the chamber is between atmospheric and 15 mTorr it is measured by KJL912161 convection gauge, which has a measurement range of 1×10^{-3} Torr to 760 Torr. When the turbo molecular pump also starts to operate the chamber pressure goes below 1 mTorr and so it is measured using an HPS 943 digital Penning ionization cold cathode gauge, which has measurement range of 1×10^{-10} Torr to 1×10^{-2} Torr. The cold cathode gauge is mounted on the top extension of the chamber. The distance between this pressure gauge and the center of the chamber is 0.25 m. The reservoir pressure is measured 0.62 m upstream of the chamber by an MKS Baratron Capacitance manometer. The propellant gas flow rate is controlled by an Omega FMA 2615A mass flow controller. The maximum possible flow rate is 5.120 sccm. Without gas flow the back pressure is 10^{-6} Torr, and the reservoir pressure is 0.9 Torr. When the gas flow rate is 1-5 sccm ($17\text{-}83 \mu\text{L/s}$), the reservoir pressure is 10-100 Torr, and the back pressure is of the order of 10^{-4} Torr.

B. MPT Device

The schematic of MPT is given in fig. 1. It is fabricated by the experimenters. The electrodes are cut out from a sheet of 99.95 % Molybdenum foil that is 100 μm thick. The upstream electrode (e_1) and the middle electrode (e_2) are 25.4 mm \times 6 mm. The downstream electrode (e_3) is 25.4 mm \times 20 mm. The dielectric is cut out from mica sheet that is 200 μm thick. The dielectric layers are 25.4 mm \times 25.4 mm. The diameter of the cylindrical cavity is 100 μm from m_1 to m_3 , and it is 330 μm in e_3 . The flute length of the 100 μm drill is about 2 mm and it can break easily when tried to penetrate more than 1 mm. The drilling is carried out at rpm of 2800. Higher rpm is desirable as the drill bit is thin. First the layers from m_1 to m_3 are assembled. They are held together by epoxy resin. Then a bore is drilled through this piece using a drill bit of diameter 100 μm . The layer e_3 is drilled separately using 330 μm drill bit. Layer e_3 and m_3 are attached using RTV 108. The holes in e_3 and m_3 are aligned by viewing them under a $\times 10$ magnifier. The mass of the assembled piece is 0.9 g and the total thickness is about 1.1 mm.

As shown in fig. 2, after machine work the MPT is attached on a lexan block using screws and nuts. A tube of 6 mm diameter feeds argon to the cavity inside the MPT through a hole in the lexan block. The hole in the lexan block that overlaps with 100 μm hole in m_1 is 0.980 mm in diameter. The exposed surfaces of the electrodes and wires are insulated with kapton tape to prevent unwanted arcing.

C. Electrical Circuit

The schematics of circuits used to operate the MPT are shown in Fig. 3. Stable operation is possible in two possible ways. As shown in fig. 3 a, e_1 is the anode, e_3 is the cathode and e_2 is at a potential between e_1 and e_3 . In fig. 3 b, e_1 is anode and e_3 is cathode whereas e_2 is floating. The power supply for e_1 is Matsusada AU-2P150- LC. It can supply maximum voltage of 2 kV and maximum current of 150 mA. The power supply for e_2 is Matsusada AU-3R-100. It can also supply maximum voltage of 2 kV, but minimum current of 100 mA. Both power supplies can be set to generate positive or negative voltages. The values of ballast resistors, R_{B1} is 160 k Ω and R_{B2} is 60 k Ω . The resistances of current view resistors (CVR) are 1 Ω each. Voltages across CVR's are measured using Radio Shack digital multimeters.

D. Ion Probe Set up

An ion probe was used to determine ion distribution in the plume. The set up is shown in fig. 4. As shown, the probe consists of a copper rod of radius 1 mm inserted into a glass tube that has 1 mm thick wall. The probe surface is biased at -100 V using Matsusada AU-3R100. As shown in fig. 5, the fringing effect is negligible at a bias voltage of -100 V. This is determined by checking the variation in ion current as the bias voltage is made increasingly negative. As the probe is made more negative it also pulls ions that may otherwise be incident outside its periphery, and so although the plume current is constant the probe records higher current when its negative bias is increased.

The probe is mounted on a linear translation feed through so that it can traverse perpendicular to the plume axis on the horizontal plane. When the probe aligns with the plume axis it is at 4.4 cm from the MPT exit. A 1 k Ω CVR and a Radio Shack digital multimeter were used to read the ion current.

E. Optical Imaging Setup

Images of the plume were captured using a Cannon PowerShot A95 camera. Typical ISO value was 200, and F number was 3.2. The camera was positioned outside the chamber at about 0.4 m from the plume. Power of the MPT and the exposure time of the camera were varied during the experiment. After an MPT burnt out, layers e_3 and m_3 were viewed under a CZM4 microscope to study the damaging effects of the hot plume on the MPT.

F. Spectroscopy Setup

Optical Emission Spectroscopy was used to determine the electronic and rotational temperatures of the plume. Emission from the plume was collected outside the chamber by a 19 cm focal length lens which was positioned about 38.7 cm from the exit of MPT. The diameter of the lens was 6.7 cm. As shown in Fig. 4, the light from the lens was focused on an optical fiber. It is a Thorlabs M29L01 fiber, which has numerical aperture (NA) of 0.39 and core diameter of 600 μm . The light from the other end of the optical fiber was collected by a lens which had focal length of 1.5 cm and diameter of 2.8 cm. It was then focused on the entrance slit of a Newport 74050 spectrometer, which had a grating of 1800 g/mm. The slit width was set to 200 μm . The detector mounted on the spectrometer is a Newport 78105 array detector, which is a 3000 element linear CCD detector with pixel size 200 μm (H) \times 7 μm (W).

The depth and width of field were determined by probing emission from an argon calibration lamp focused into a pinhole that had a diameter of 100 μm , and they were found to be 3.03 cm and 360 μm respectively. The distance between the source and the lens was approximately 41 cm. The lens and optical fiber were mounted on a translation stage, which could move them to the left and right (x-axis) of the pin hole or towards and away (y-axis) from the pin hole. The relative distance between the lens and the fiber is fixed as they are attached to the translation stage so that it displaces the lens and the fiber in unison relative to the source. The least count of the translation stage was 20 μm . The data obtained from this procedure are shown in figs. 7.

Fig. 7a shows the counts recorded from the pin hole as the translation stage carries the lens and fiber along the x-axis. 'Integrated counts' is calculated by integrating the area under the line emission at 811 nm. Gaussian fit is applied to the data shown in fig. 7a to estimate the FWHM. The probe size, which is the resolution of the width of region viewed by the optical system, is defined to be equal to the FWHM of the curve fit. Hence, the probe size is 360 μm .

Fig. 7 b shows the counts recorded from the pin hole as the collection optics is moved in the y-direction from the pin hole. Lorentzian fit is performed on the data in fig 7 b to estimate the FWHM, which is defined as the depth of field of the optical system. From the curve fit, the depth of field is 3.03 cm.

The plume spectra were recorded from the region 2 mm downstream of the exit plane. There the length of the visible plume perpendicular to its axis is estimated to be less than 3.03 cm. This means the lens collects light over the entire depth of the plume during spectroscopy experiments.

The recorded intensities of the emissions were calibrated using a CI-system SR-20 cavity blackbody that can reach maximum temperature of 1200 $^{\circ}\text{C}$. The wavelengths of the spectra were calibrated by recording known lines from Argon and Mercury lamps. As shown in fig. 8, according to 546 nm line recorded from the Mercury lamp, the spectral resolution is 0.452 nm.

III. Results and Discussion

Stable operation modes of the MPT were determined. Its current, voltage and power characteristics were recorded. Visual features of the plume were also studied. The results also helped to understand the factors that lead to deterioration of the MPT during operation. The data was also used to infer the composition of the plume and its electronic excitation temperature. The following section presents the results and their interpretation.

G. Optical Imaging

As shown in fig. 9, the plume rapidly expands into the chamber. The pictures are taken with 2.5 s exposure time when the argon flow rate was 5 sccm for input powers of 40 mW, 291 mW and 531 mW. There is a structure in the appearance of the plume. It has a luminous core anchored at the exit. The core typically extends about 1.5 mm downstream, and then transitions to a faint bluish region. The variation in

the brightness of the plume over its length is affected by its expansion and the lifetime of the excited species in the plume. In addition, the presence of a shock wave may also shape its visual structure.

The MPT is operated as a highly under-expanded jet as the pressure at exit is ~ 1 Torr and the pressure in the chamber is $\sim 10^{-3}$ Torr, and so the plume is expected to have a barrel shock. The luminous core of the plume could be the region inside the barrel shock. The transition from luminous core to the faint bluish region could be consequences of the presence of the Mach disk and oblique shocks. The pressure and density rise behind a shock. This could increase the rate of quenching collisions. This implies that the excited species are quenched behind the shock and they stop emitting which leads to a faint region downstream of the luminous core.

Schlieren imaging using 3 ft focal length mirror was attempted on the plume, but it did not reveal the expected density gradients. Schlieren imaging could not even distinguish the plume from the background gas. Clearly the set up that was used was not sensitive enough. The lack of sensitivity of the set up that was used can be understood from the formula for relative intensity variation. The relative intensity variation in Schlieren method is given by

$$\frac{\Delta P}{P_i} = \frac{f_2}{a} \int_{\Delta z} \frac{1}{n} \frac{\partial n(x, y, z)}{\partial y} dz \quad (1)$$

, where

$$P_i = I_i b a$$

, and

$$\Delta P = I_i b \Delta a.$$

I_i is the intensity of the image at the focal plane in the absence of plume, and b, a are the width and height of the image at the focal plane; Δa is the size of deflection of image in the focal plane because of refractive index of the plume; f_2 is the focal length of the mirror that focuses light on the knife edge; n is the refractive index of the plume which is related to density by

$$N = 1 + K\rho \quad (2)$$

Here, K is called the Gladstone constant and ρ is the density of the medium. The lack of sensitivity of Schlieren method for plume diagnostics arises mainly from the smallness of ΔZ , which is the depth of the plume along the optical path. The sensitivity will also improve by using a mirror of longer focal length.

The change in the length of the luminous core as the MPT power and flow rate are varied is shown in fig. 10. The length was determined by multiplying the length of the luminous section in the photograph by the ratio of the real length of the lexan block to its length in the photograph. According to this data, the length of the core is independent of the flow rate. It increases almost linearly with power.

Images of e_3 and m_3 were taken after an MPT stopped functioning. As shown in Fig. 11 they reveal that the electrodes melt and erode during operation. The melted part of the electrode settles on the dielectric. The MPT stops to function when the meltdown clogs the cavity. The shape and size of the holes were also distorted after repeated usage.

H. Operation Modes

The performance of MPT depends on the relative potentials of the electrodes. There were minimum fluctuations in the electrode currents and plume intensity when e_1 was set as anode, e_3 as cathode and e_2 was floating. When anodes and cathodes were reversed in this configuration- that is e_3 was set as anode,

e_1 was set as cathode and e_2 floating, the required breakdown voltage was about 1500 V; when the plume appeared it quickly damaged the MPT and made it defunct so that it was not possible to study this configuration. When e_2 was also powered the discharge was confined between e_1 and e_2 and a plume was not observed. After repeated operations in the configuration in which e_1 , e_2 and e_3 were set at monotonically decreasing potentials, e_2 and e_3 short circuited and a bright plume, which was relatively stable, was observed. In this relatively stable configuration, e_2 was effectively floating because current flow was predominantly in e_1 and e_3 only. It was not possible to generate a plume by an external short circuit between e_2 and e_3 . We believe that multiple operation of MPT melts the area of electrodes exposed to the discharge inside the MPT. When the melted part settles between e_2 and e_3 , the e_2 becomes effectively floating; current flows in e_1 and e_3 and a relatively stable plume is observed. After the most stable configuration was determined, e_2 was deliberately left floating, and the MPT and its plume were characterized. In this configuration, plume can be generated in a new MPT so that it is not necessary to operate it multiple times to generate the plume. In other configurations it was not possible to study the plume and the currents in the electrodes as they were either not stable or the break down voltage was too high.

I. Electrical Characteristics

When e_1 , e_2 and e_3 are set at monotonically decreasing potentials their currents are shown in fig. 12. In this configuration, the discharge is confined between e_1 and e_2 . A visible plume is not observed. Current in e_3 (I_3) is almost zero. Almost all current flows from e_1 to e_2 . When the voltage is further increased the plume starts to flicker and I_3 increases. Currents in all the electrodes (I_1 , I_2 , I_3) become unstable, and it is no longer possible to record the current-voltage characteristics. Multiple operations lead to an internal short circuit between e_2 and e_3 . fig. 13 shows the currents when e_2 and e_3 have an internal short circuit and e_2 was not powered. fig 14 shows currents in e_1 and e_3 when e_2 was left floating and there was no short circuit between e_2 and e_3 .

I_1 and I_3 are higher in fig. 13 than in fig. 14 possibly because when e_2 and e_3 are internally short circuited they act as single thicker cathode. The currents in successive runs decrease possibly because of the erosion of cathode during operation. When all three electrodes are powered, and the plasma is confined between e_1 and e_2 , the erosion of e_2 first leads to internal short circuit between e_2 and e_3 . This increases the current as the effective cathode is now thicker. After current starts to flow in e_3 , its erosion leads to decrease in current values in successive runs. The plots show that the typical current in MPT was ~ 0.1 mA and voltage input was ~ 1000 V.

Fig. 15 shows the variation in the power of MPT as supply voltage and flow rate are increased. Typical operating power is between 50 and 500 mW. For a given supply voltage the power increases when the flow rate increases. When flow rate increases the current in the MPT can also increase because of the increase in the flux of atoms or it can decrease because the pressure increases with flow rate and an increase in pressure increases collision frequency. Current density, J is given by

$$J = nqV_d \quad (3)$$

$$= nq\mu E$$

$$J = nq^2 E / mv \quad (4)$$

, where n is the number density of charge carriers, q is the charge, V_d is the drift velocity, μ is the mobility, E is the electric field strength, m is the mass of the charge carrier and v is the momentum exchange collision frequency. Hence, J is inversely proportional to v . According to fig. 15, in MPT an increase in flow rate at a given supply voltage results in an increase in current and power, which implies that the increase in the number density of charge carriers in the MPT outweighs the increase in collision frequency.

J. Ion distribution in the plume

Measurements carried out by the ion probe are represented in fig. 16. According to fig. 16 a, the typical ion flux is $1\mu\text{A}/\text{cm}^2$. The off-axis angle is defined as the angle between the plume axis and the probe's line of sight of the MPT exit. Such low ion content in the plume is not surprising given that the power input is 250 mW. It can be shown that at least 5.09 W is necessary to fully ionize Ar flow at 5 sccm to Ar^+ even if all the input energy were to go into ionization.

Fig. 16 b contains the same data as fig. 16 a except that now the horizontal axis is the distance over which the probe travels. Total ion current in the plume calculated from the curve fit on fig. 16 b is $17.0\mu\text{A}$. The calculation of total ion current assumes that the ion current has a Gaussian distribution over the cross section. It can be shown that the total ion current

Assuming that all the ions are Ar^+ , the ratio of ion flow rate to flow rate of neutral species in the plume is 5.2×10^{-3} . Assuming that all the ions in the discharge are also Ar^+ , the ratio of ion current in the plume to discharge current turns is 5.6×10^{-2} .

The low proportion of ion content implies that most of the thrust comes from gas dynamic expansion rather than ion acceleration.

K. Spectroscopy

Line emissions from molybdenum, argon ions and excited neutral species of argon were detected between 405 nm and 827 nm. Mo lines were predominant between 500 nm and 650 nm. Ar^+ lines were identified at 434 nm, 611 nm and 617 nm. Most of the recorded line emissions were from excited neutral species of Ar and from Mo. The presence of Mo species in the plume implies that some of the exposed areas of Mo electrodes are evaporated and carried away by the plume. It was not possible to identify all the lines that were recorded because the spectral resolution was 0.452 nm. Especially at wavelengths below 600 nm there are relatively strong emissions from Mo and Ar^+ , but they could not be distinguished from one another. Parts of spectrum are shown in fig. 3.12. Doppler fit has been applied to some of the lines. The fitted spectrum is used to calculate the intensity from a given line emission which is necessary to calculate the electronic excitation temperature as explained in the next section.

L. Determination of temperature

The electronic excitation temperature was inferred by Boltzmann fit on the plot of $\ln[I/gAv]$ vs. ϵ/k , where I is the intensity of the line, g is the degeneracy of the upper level of energy transition, A is the Einstein coefficient, ν is the frequency of transition, ϵ is the transition energy and k is the Boltzmann constant. For a given value of ν the values of g , A and ϵ were obtained from the NIST database. I is calculated by integrating the area under the Doppler fit on spectral lines. The gradient of line fit on $\ln[I/gAv]$ vs. ϵ/k is equal to $-1/T$, where T is the electronic excitation temperature.

Molybdenum temperature could not be determined as the energy states could not be identified. The energy levels of metals are closely spaced and it is often difficult to distinguish them.

As shown in figs. 18, the electron temperature inferred from data on neutral species is 1270 K, and the electron temperature inferred from ions is 3510 K. The values of temperatures obtained here are much lower compared to the expected electron temperatures inside the discharge, where the charged species are accelerated over a potential difference of ~ 1000 V. This means the electronic excitation of the atoms and ions that gave rise to the recorded spectra happened in the after glow i.e. outside the MPT. As mentioned above, the probe region was located 2 mm downstream from the exit plane. Free electrons cannot reach that far from the discharge by convection so the inferred temperature cannot possibly indicate electron population distribution at the probe region. The ions and neutral species were excited somewhere upstream of the probe region, and they reached the probe region by convection so the values of temperature given here provides an idea of electron population distribution upstream of 2 mm in the after glow. The maximum error in the calculation arises from the noise in black body signal used to calibrate the intensity. The fact that the line fit does not pass between all the maximum and minimum

values of $\ln[I_{ji}/A_{ji}g_jv_{ji}]$ indicates that the Ar and Ar⁺ species in the plume do not have equilibrium distribution.

IV. Conclusion

In this way, MPT is an electro-thermal micro propulsion device, which was designed and studied with the goals of minimizing its size, mass, operating power and propellant consumption. The MPT was successfully operated at low flow rates of ~ 1 sccm. The most stable operation is attained when the upstream electrode e_1 is anode, the downstream electrode e_3 is cathode and the middle electrode e_2 is floating. The MPT operates as an electrothermal thruster because most of the momentum thrust of the MPT is generated by the expulsion of hot neutral argon atoms. Measurements from ion probe revealed that there is also low proportion of ions in the plume; therefore, MPT is able to expel ions without the use of an external magnetic field or an external electron emitter. Comparison of current voltage characteristics of the MPT with the ion probe measurements show that the net ion current in the plume is also considerably less than the discharge current. The ion content in the plume was also detected by emission spectroscopy. The detection of Molybdenum atoms by spectroscopy implies that the plume melts and evaporates the exposed regions of the electrodes. The magnified view of the exit hole in e_3 and m_3 also reveal that the holes are distorted and enlarged by the time the MPT becomes defunct. The electronic excitation temperature of the ions and neutral species were found to be 3510 K and 1270 K respectively. The thrust from the MPT is yet to be determined. The material selection issue for the electrodes also needs to be addressed in future.

References

- [1] Lewin A. "Evaluating the present and potential future impact of small satellites," 18th Annual AIAA/USU Conference on Small Satellites, Aug. 2004.
- [2] Khayms V. and Martinez-Sanchez M., "Design of a Miniaturized Hall Thruster for Microsatellites," AIAA Paper 96-3291, 32nd AIAA Joint Propulsion Conference, Lake Buena Vista, FL, 1996.
- [3] Monheiser J., Hraby V. and Freeman C., "Development and testing of a low-power Hall thruster system." Chapter 10 in *Micropropulsion for Small Spacecraft*, eds. M.M. Micci and A.D. Ketsdever, Progress in Aeronautics and Astronautics, Vol. 187, 2000.
- [4] Patterson M., "Low-power ion thruster development status," AIAA Paper 98-3347, 34th Joint Propulsion Conference, Cleveland, OH, July 1998.
- [5] Gorshkov O., "Low-power Hall type and ion electric propulsion for small sized spacecraft," AIAA Paper 98-3929, 34th Joint Propulsion Conference, Cleveland, OH, July 1998.
- [6] Spangers G. G., White D., Schilling J., Bushman S., Lake J. and Dulligan M., "AFRL microPPT development for the TechSat21 flight," IEPC Paper 01-166, 27th International Electric Propulsion Conference, Pasadena, CA, 2001.
- [7] Marcuccio S., Genovese A., Andrenucci M., Bartoli C., Gonzalez J. and Saccocia G., "Field emission electric propulsion (FEED) system study," IEPC Paper 93-156, 23rd International Electric Propulsion Conference, 1993.
- [8] Martinez-Sanchez M. and Pollard J., "Spacecraft electric propulsion – An overview," *Journal of Propulsion and Power* 14:688-699, 1998.
- [9] Bzibziak R., "Miniature cold gas thrusters," AIAA Paper 92-3256, 28th Joint Propulsion Conference, Nashville, TN, July 1992.
- [10] Edwards, I. and Jansson, R. E. W., "Gas dynamics of resistojets," *Journal of the British Interplanetary Society*, 24:729-742, 1971.
- [11] Barber H. E., Falkenstein G. L., Buell C. A. and Gurnitz, R. N., "Microthrusters employing catalytically reacted N₂-O₂-H₂ gas mixtures, Tridyne," *Journal of Spacecraft and Rockets*, 8:111-116, 1971.

- [12] Raizer, Yu. P., *Gas Discharge Physics*, Springer, New York, 1991.
- [13] Ito T., Gascon N., Crawford W. S. and Capelli M. A., "Further Development of a Micro Hall Thruster," AIAA Paper 2006-4495, *42nd Joint Propulsion Conference*, Sacramento, CA, July 2006.

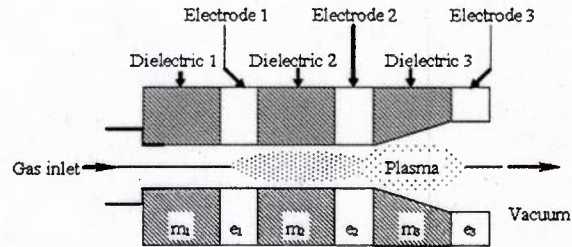


Figure 1. The schematic of MPT.

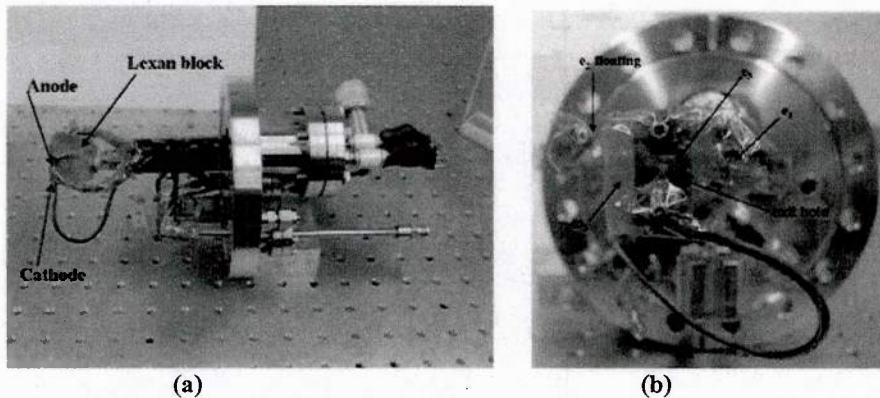


Figure 2. (a) Side view of the MPT assembly that is placed inside the vacuum chamber. (b) . Front view of the MPT assembly.

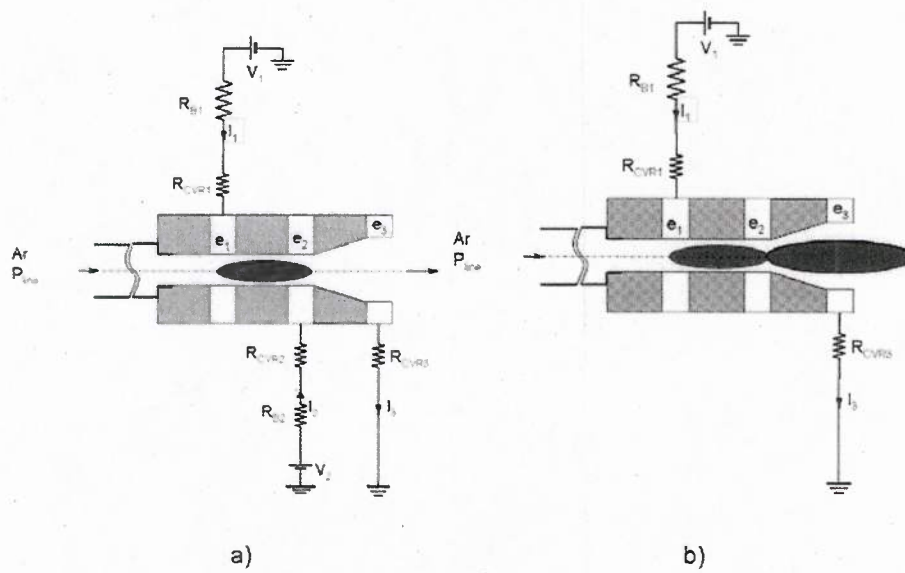


Figure 3. Electrical circuit of MPT. (a) Middle electrode, e_2 is not floating. (b) Middle electrode is floating.

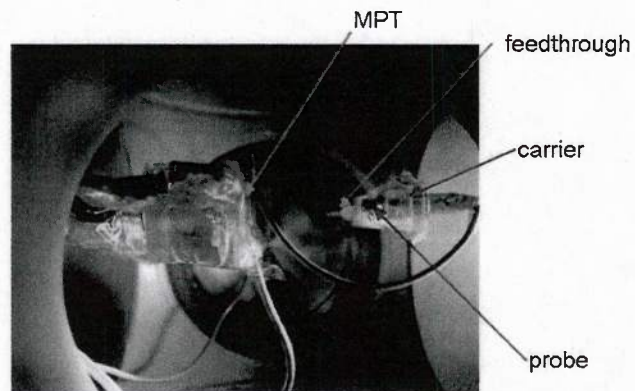


Figure 4. Ion probe set up inside the vacuum chamber.

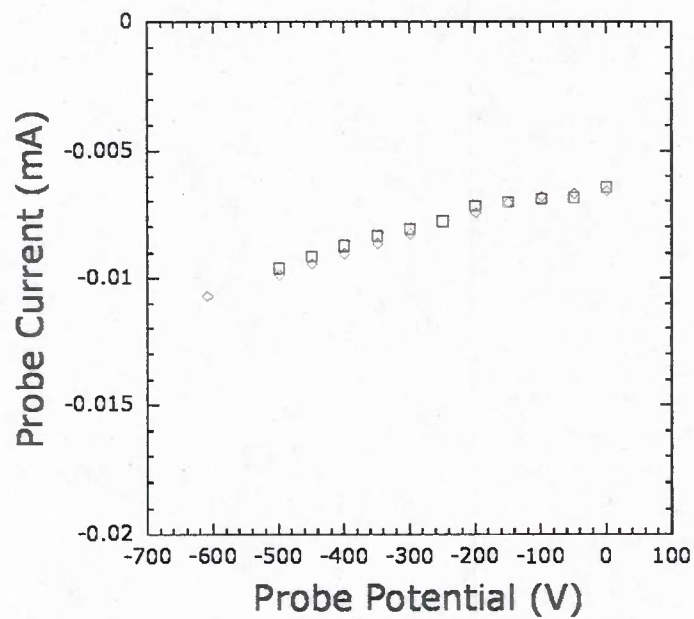


Figure 5. Fringing effect. The power input to the MPT is constant, but the current recorded by ion probe increases as it is made more negatively biased.

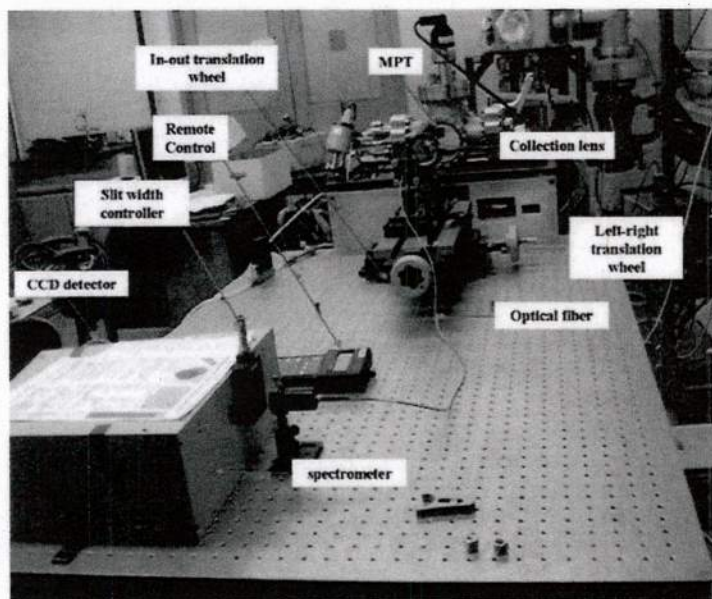


Figure 6. The set up for emission spectroscopy.

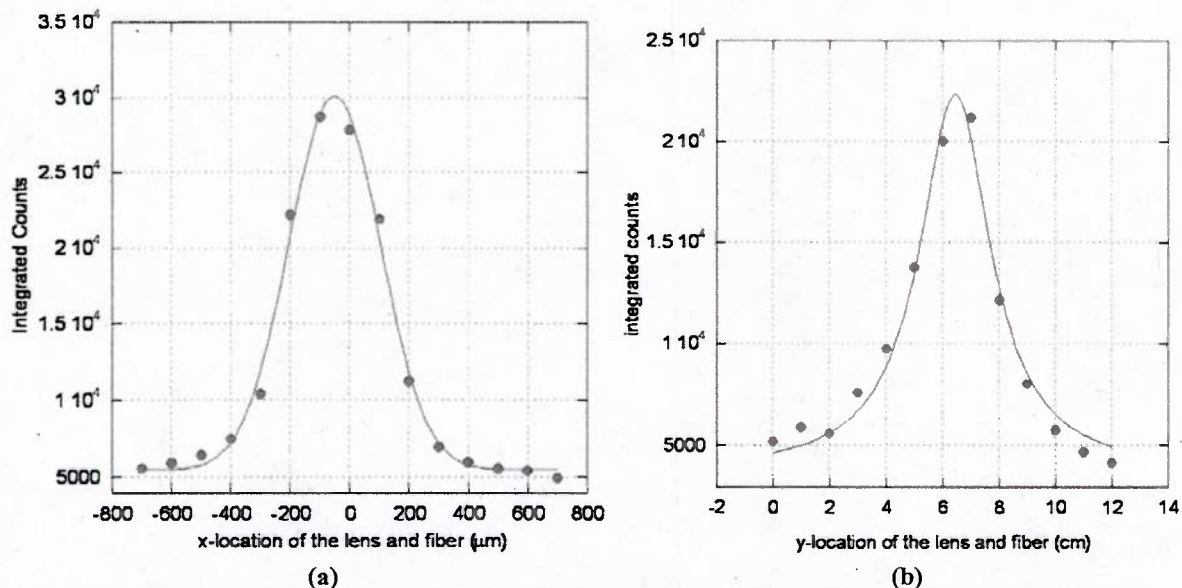


Figure 7. (a) Determination of probe size. Integrated counts is the area under the line emissions at 811 nm wavelength from an argon calibration lamp. (b) Determination of depth of field. Integrated counts is the area under the line emissions at 811 nm wavelength from an argon calibration lamp.

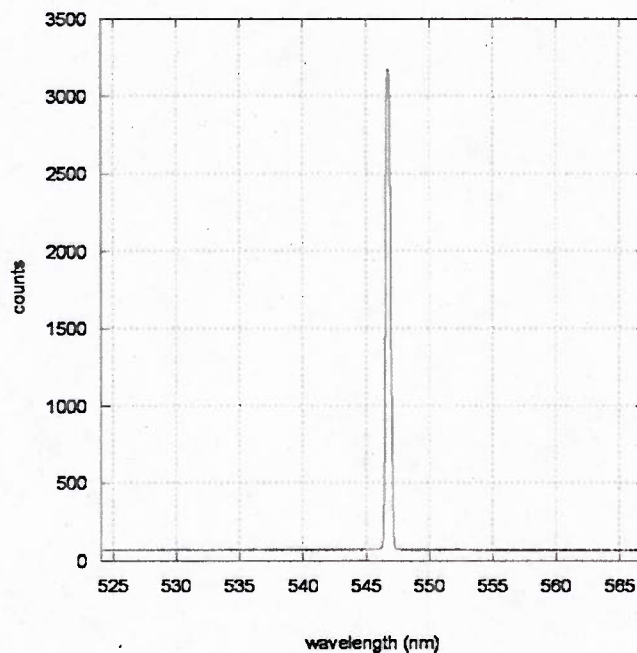


Figure 8. 546 nm line recorded from mercury calibration lamp. FWHM is 0.452 nm. Slit width of the spectrometer was 200 μm .

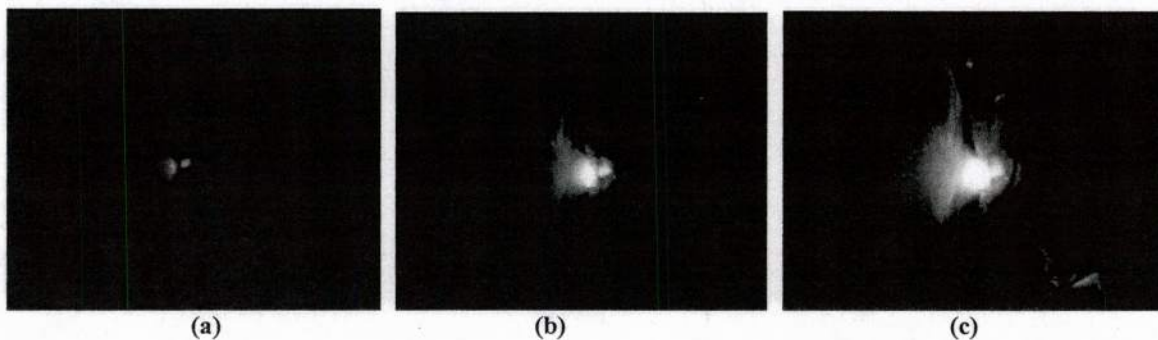


Figure 9. (a) Plume image with 2.5 s exposure time. Input power is 40 mW, and the luminous length is 0.56 mm. (b) Plume image with 2.5 s exposure time. Input power is 291 mW, and the luminous length is 1.2 mm. (c) Plume image with 2.5 s exposure time. Input power is 531 mW, and the luminous length is 2.2 mm.

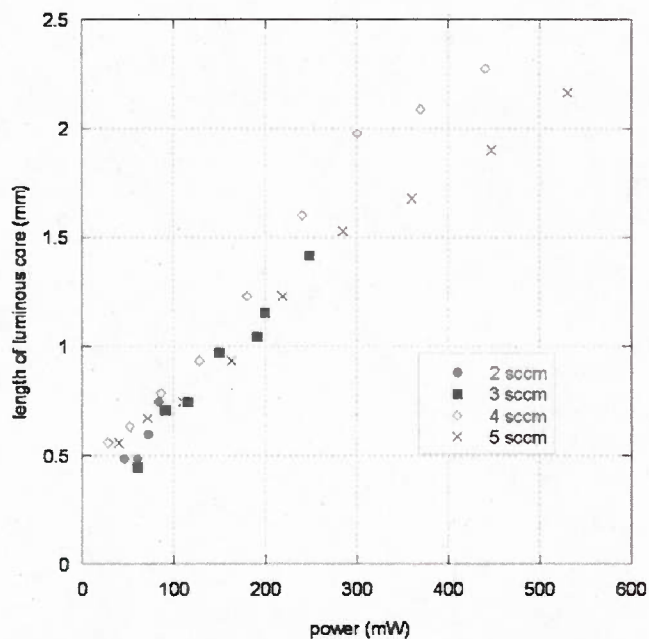


Figure 10. Variation in the length of the luminous core of the plume as the power and flow rate are changed. The length of the core increases almost linearly with the power. It is independent of the flow rate.

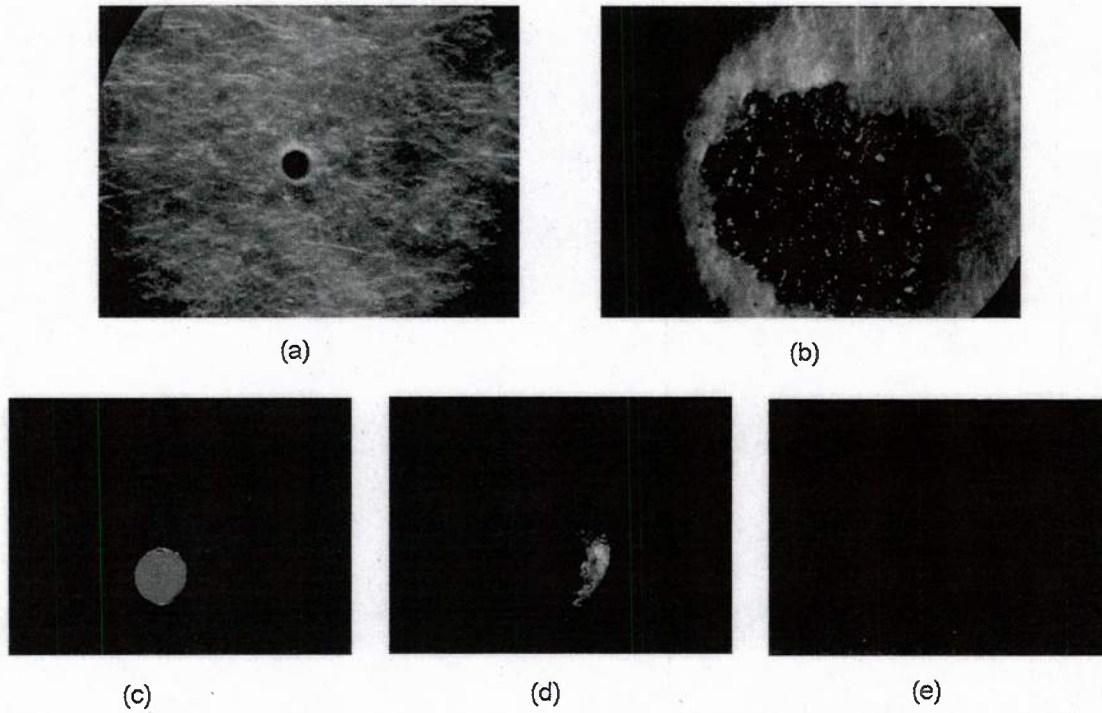


Figure 11. a) m_3 before running MPT. b) e_3 after MPT stops functioning. c) e_3 before running MPT. d) downstream face of e_3 after MPT stops functioning. e) upstream face of e_3 after MPT stops functioning.

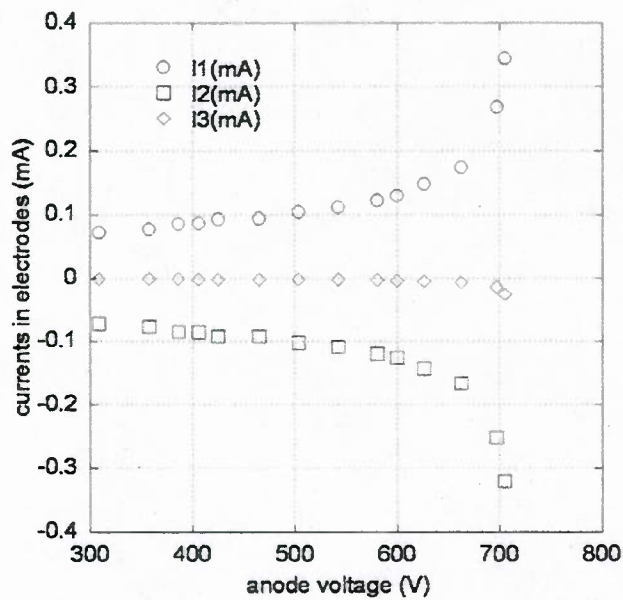


Figure 12. MPT current vs. voltage when all three electrodes are powered.

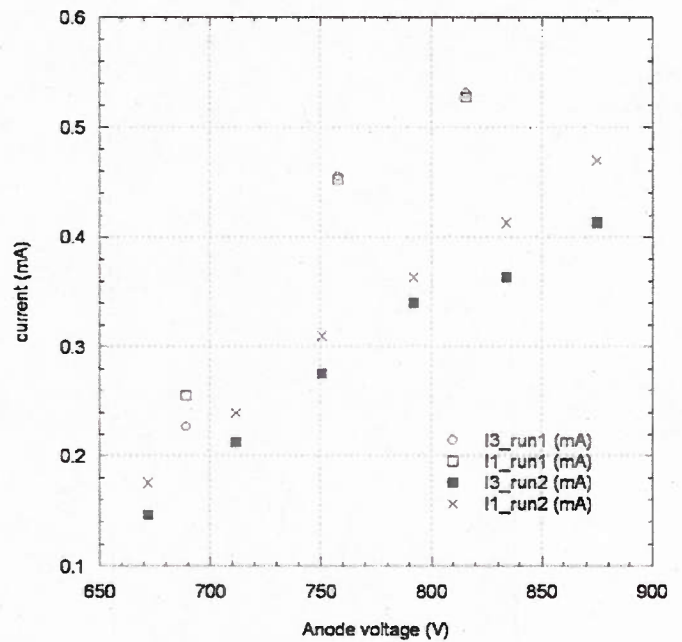


Figure 13. MPT current vs. voltage when there is internal short circuit between e_2 and e_3 .

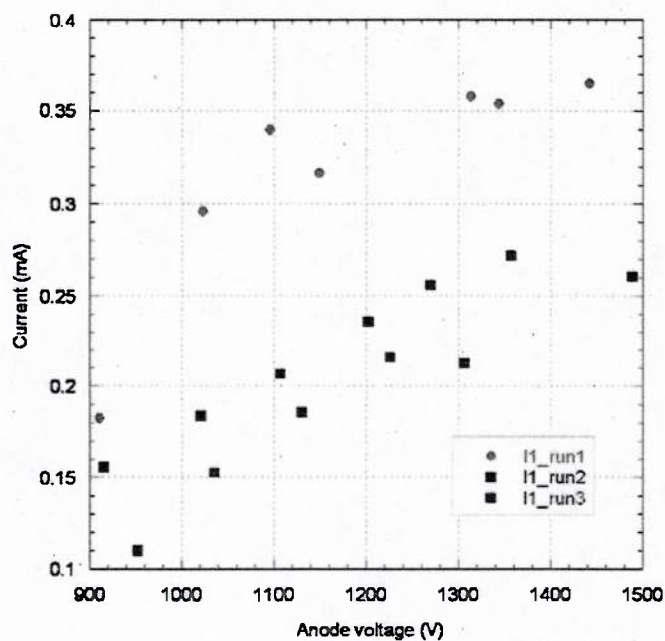


Figure 14. MPT current vs. voltage when e_2 is floating.

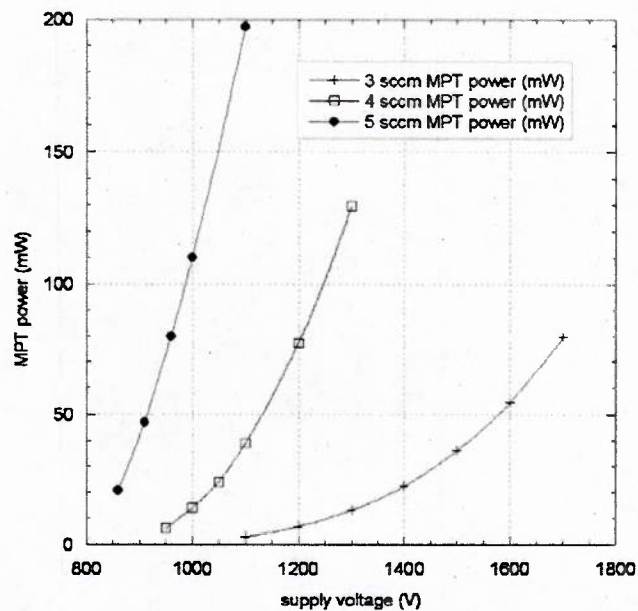
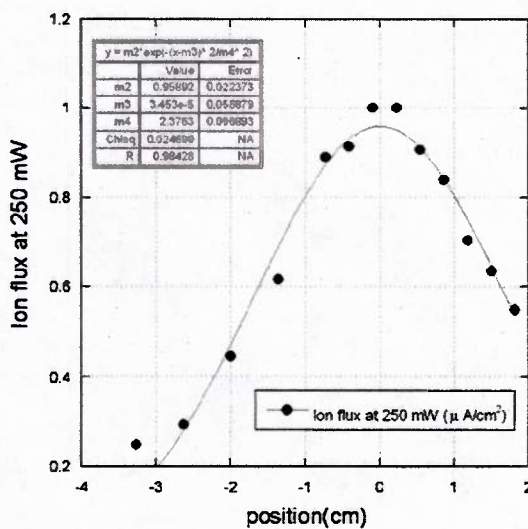
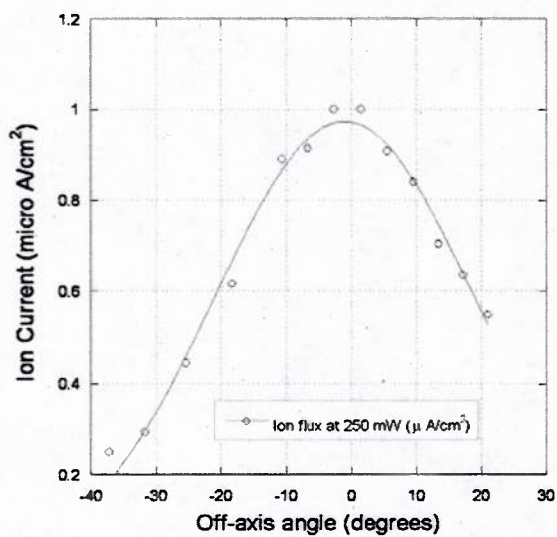


Figure 15. MPT power vs. voltage at given flow rates.



(a) Ion flux vs. off-axis angle. (b) Ion flux vs. distance travelled by the probe.

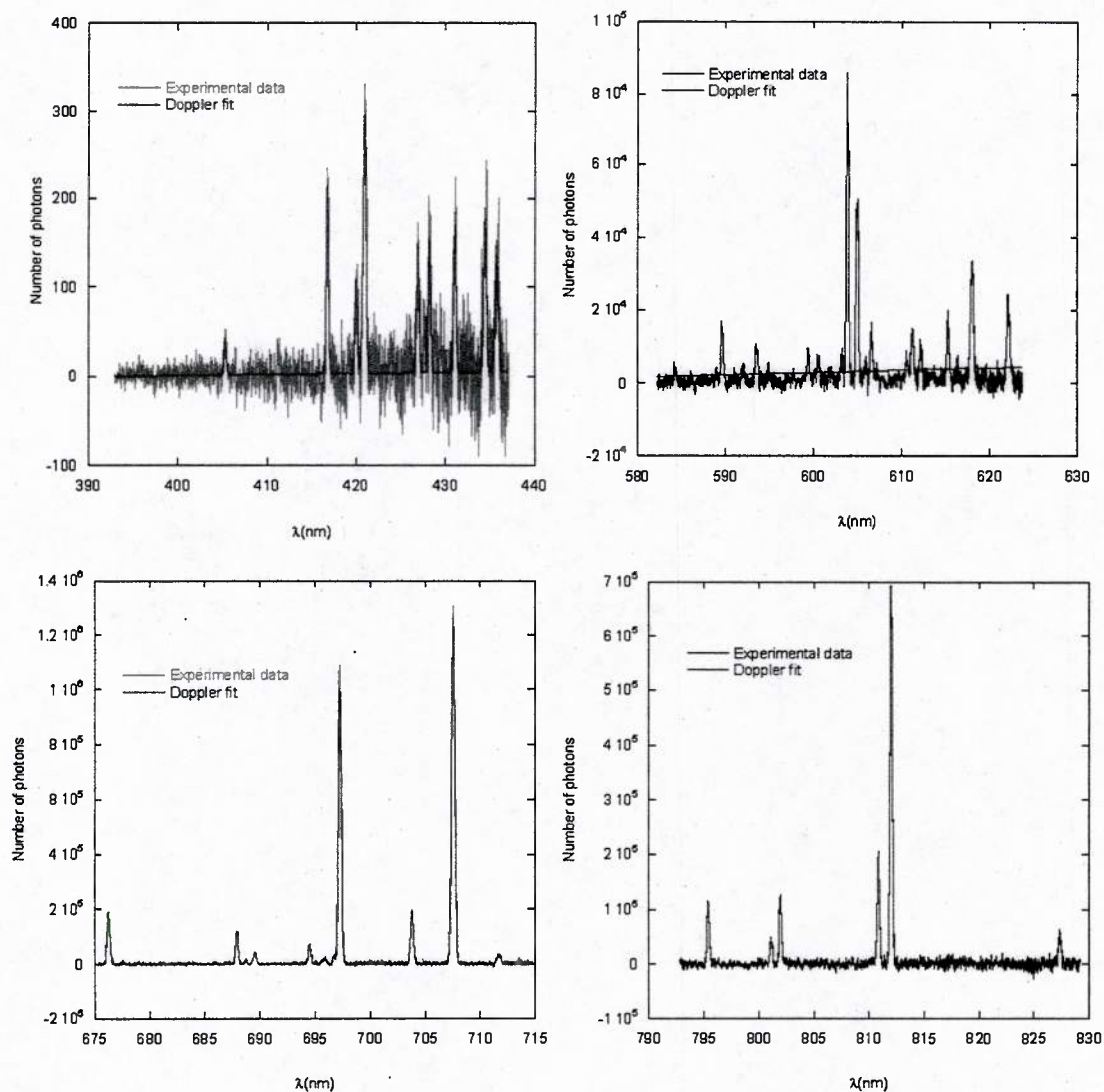


Figure 17. Some spectra from plume emissions. The Doppler fit is used to calculate the total intensity from a given line emission.

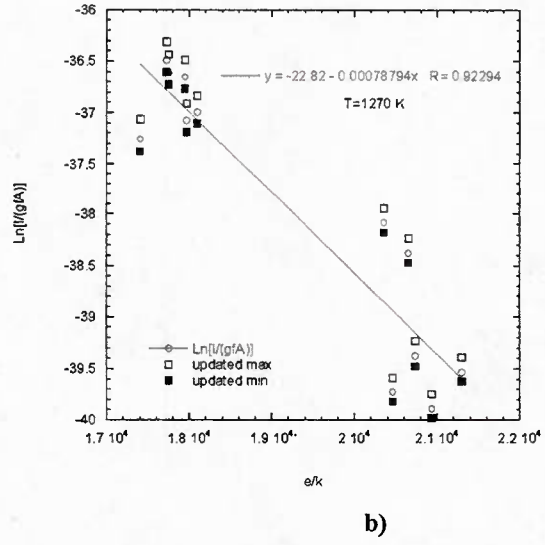
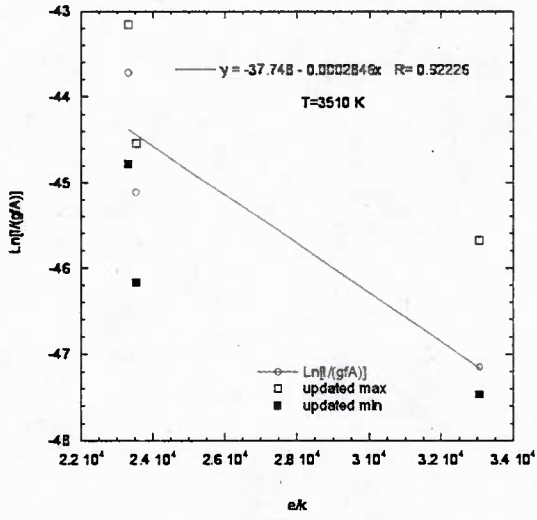


Figure 18. a) Determination of electronic excitation temperature of Ar^+ . b) Determination of electronic excitation temperature of Ar .

Computational Investigation of Micro Plasma Thruster (MPT)

I. Introduction

Small satellites (mass less than 100 kg) have recently gained interest for various commercial, military, and science space missions.¹⁻² Several advantages, including a reduced launch cost are realized with small satellites. Small satellites are power-limited, typically delivering less than a watt per kilogram of spacecraft mass. Propulsion requirements for these small satellites can vary significantly given the diversity of small satellite missions, but are generally characterized by their very low thrust values (\sim mN) and low impulse bits for attitude control (~ 10 's μ N-s). Scaling traditional propulsion systems down in power and size to suit the needs of small satellites is a major engineering challenge.

Cold gas thrusters are low-performance devices limited by low values of specific impulse (~ 50 s).³ Advantages of these devices compared to other propulsion systems include their low system complexity, low-cost, and absence of satellite contamination problems when using inert propellants (e.g. N_2). Micronozzle cold gas thrusters are suitable for attitude control applications of small satellites. They can also be used as primary propulsion system if the Δv requirements are less than ~ 100 m/s. Since nozzle throat diameters in the micrometer range are required for micronozzle propulsion, the production of these microthrusters rely on MEMS fabrication technologies.⁴⁻⁶

The extremely small dimensions of microdischarges combined with intense and controllable gas heating can be exploited in microthrusters technologies. Like conventional cold gas thrusters, electrothermal microdischarge propulsion systems can have extremely low mass and volume footprints. They are electrically simple, and, unlike other electric propulsion technologies, they do not require auxiliary systems such as neutralizers, heaters, or magnets. The thrust from these devices is widely tunable by varying power levels. A significant improvement in the specific impulse compared to conventional micronozzle cold gas thrusters can potentially be achieved with these systems.

The Micro Plasma Thruster⁷ (MPT) concept consists of a direct-current microdischarge in a geometry comprising a constant area flow section followed by a diverging exit nozzle. Geometric dimensions are on the order of hundreds of microns. In the MPT concept, a stable microdischarge is generated at low propellant flow rates (few sccm). The propellant gas in the microdischarge is eventually expelled from the diverging nozzle. Thrust is produced by the expanding gas flow, which is heated by the microdischarge. The MPT has potentially important advantages over competing concepts such as the micro resistojet thruster⁸, which also relies on preheating an expanding gas stream. The important difference between a resistojet and the MPT is the nature of power deposition into the gas. In a resistojet, the heating element is essentially the hottest part of the system and heat addition to the gas occurs via conduction/convection to the gas stream. There is clearly an upper limit on the heating element temperature which in turn limits the amount of heat delivered to the gas. In the MPT, the gas is heated directly by the plasma. Importantly, if the plasma thermal power deposition occurs far away from the surfaces, much higher thermal energies can be delivered to the gas.

Successful design of the microthruster requires a detailed understanding of microdischarge phenomena as well as plasma-flow interactions. Experimental investigations of the microdischarge are hindered by the extremely small geometries, where well-established plasma diagnostic techniques are not applicable. High-fidelity computational models can therefore have a big impact in developing a fundamental understanding of the MPT.

In previous studies, Kothnur and Raja⁹ studied direct-current microdischarges in a flowing gas stream for applications in electro-thermal microthrusters. For currents around 1 mA, the microdischarge is found to operate in an abnormal glow mode with positive differential resistivity. An increase in input electrical power results in almost linear increase in the gas temperatures; this property of microdischarges is a key

feature that can be exploited in the MPT concept. Arakoni *et al*¹⁰ studied a nominal microdischarge configuration with a flowing gas that resembles a thruster, although the flow modeling approach provides an inadequate description of the gas dynamics expansion through the nozzle and subsequent expansion into vacuum. Gas temperatures exceeding 1000 K are reported for power densities of 10's kW/cm³ at upstream pressure of tens of Torr. They found that the nozzle length and the location of the discharge in the nozzle have an important influence on the incremental thrust (above that of the cold flow).

Section II describes the mathematical model and numerical approach used in this study. The model comprises a plasma module coupled to a flow module. The plasma module provides a self-consistent, multi-species, multi-temperature description of the microdischarge phenomena while the flow module provides a description of the low Reynolds number compressible flow through the MPT. Section III describes simulation results and a discussion of the MPT phenomena. Finally, we conclude in Section IV.

II. Methodology

Coupled plasma and gas flow phenomena are encountered in a number of applications requiring the development of an integrated plasma model coupled to a gas dynamic flow model.¹¹ In the MPT, the microdischarge plasma is in a highly non-equilibrium state with disparate electron and gas temperatures and non-equilibrium finite-rate chemical effects. The gas flow is characterized by low-Reynolds number viscous dominated effects combined with high Mach number compressibility effects owing to the expansion of the relatively high-pressure (~100 Torr) micronozzle gas stream into vacuum. Both the plasma and flow phenomena are strongly coupled: the plasma causes gas heating, which modifies the gas density, and hence the flow field; the gas flow velocities, in turn, affects the distributions species and temperature of plasma in the discharge. The integrated plasma-flow model used in this study is described below.

III. Plasma Module

i. Governing Equations

The densities of individual species in the discharge are determined by the species continuity equation,

$$\frac{\partial n_k}{\partial t} + \bar{\nabla} \cdot (n_k \bar{V}) + \bar{\nabla} \cdot \bar{\Gamma}_k = \dot{G}_k \quad k = 1, \dots, K_g (k \neq k_b), \quad (1)$$

where n_k is the number density of species k , \bar{V} is the mass-averaged gas flow velocity, $\bar{\Gamma}_k$ is the drift-diffusion flux of species k , \dot{G}_k is the gas-phase species generation rate through plasma chemical reactions, and K_g is the total number of gas species. A dominant neutral species is identified as the “background” species, and is designated as k_b ; its density being determined to satisfy the ideal gas law,

$$P = n_{k_b} k_B T_g + n_e k_B T_e + \sum_{k \neq k_e, k \neq k_b} n_k k_B T_g, \quad (2)$$

where P is the local pressure, k_B is Boltzmann's constant, subscripts e and g denote electrons and the background gas, respectively.

The electron temperature, T_e , is explicitly computed in order to determine the reaction rates due to electron impact and the electron transport properties. For this purpose, the following electron energy equation is solved,

$$\begin{aligned}
& \frac{\partial}{\partial t} \left(\frac{3}{2} k_B n_e T_e \right) + \vec{\nabla} \cdot \left(\frac{5}{2} k_B n_e T_e \vec{V} \right) + \vec{\nabla} \cdot \left(\frac{5}{2} k_B T_e \vec{\Gamma}_e \right) - \vec{\nabla} \cdot (\eta_e \vec{\nabla} T_e) \\
& = e(\vec{\Gamma}_e + n_e \vec{V}) \cdot \vec{\nabla} \phi - \frac{3}{2} k_B n_e \frac{2m_e}{m_{k_b}} (T_e - T_g) \bar{\nu}_{e,k_b} - e \sum_{j=1}^{I_g} \Delta E_j^e r_j
\end{aligned} \tag{3}$$

where η_e is the thermal conductivity of electrons, m_e and m_{k_b} are the molecular mass of electron and dominant background gas respectively, $\bar{\nu}_{e,k_b}$ is the electron momentum transfer collision frequency with the background gas, ΔE_j^e is the energy lost per electron (in eV) in an inelastic collision event represented by a gas-phase reaction j , r_j is the rate of progress of a reaction j , and I_g is the total number of gas-phase reactions. In our model, we assume a common temperature for all heavy species (ions and neutrals), this temperature being solved for in the flow module.

The self-consistent electrostatic potential is determined using the Poisson's equation,

$$\nabla^2 \phi = -\frac{e}{\epsilon_0} \sum_k Z_k n_k, \tag{4}$$

where ϕ is the potential, e is the unit electric charge, ϵ_0 is the permittivity of free space, and Z_k is the charge number of species k (e.g., -1 for electrons).

The ion flux is evaluated as $n_i \vec{V} + \vec{\Gamma}_i = n_i \vec{u}_i$, where \vec{u}_i is the ion fluid velocity, which is determined using the first moment of the ion species Boltzmann equation, i.e., the ion species momentum equation,

$$\frac{\partial n_i \vec{u}_i}{\partial t} + \vec{\nabla} \cdot (n_i \vec{u}_i \vec{u}_i) = -\frac{Z_i e n_i}{m_i} \vec{\nabla} \phi - \frac{k_B T_i}{m_i} \vec{\nabla} n_i - n_i (\vec{u}_i - \vec{V}) \bar{\nu}_i. \tag{5}$$

The first term on the left-hand side of Eq. (5) is the unsteady term and the second term is the ion inertia term which is non-negligible as the pressure approaches vacuum conditions near the MPT exit. The first term on the right-hand side of Eq. (5) is the electrostatic force on the ion fluid, the second is the gradient diffusion of ion fluid momentum, and the last term is the loss of ion fluid momentum owing to collisions (friction) with other species. The last term assumes that the ion density is small compared to the dominant background species density, whose fluid velocity corresponds to the mean-mass velocity of the gas. In Eq. (5), T_i is the ion temperature, which is assumed equal the local heavy species (gas) temperature T_g and $\bar{\nu}_i$ is the ion momentum-transfer collision frequency. The mass-averaged flow velocity and the gas temperature are solved for using the flow module discussed in the next section.

ii. Transport Formulation

For species other than the ions (neutrals and electron), species number flux is evaluated using the drift-diffusion approximation, given as,

$$\vec{\Gamma}_k = -\mu_k n_k \vec{\nabla} \phi - D_k \vec{\nabla} n_k, \tag{6}$$

where, $\mu_k = Z_k e / m_k \bar{\nu}_k$ is the charged species mobility and $D_k = k_B T_k / m_k \bar{\nu}_k$ is the species diffusion coefficient. The electron thermal conductivity appearing the electron energy equation is given as

$\eta_e = (5/2)n_e D_e$. The operating (propellant) gas considered for this study is argon. The electron transport properties are determined apriori by solving a zero-dimensional electron Boltzmann equation ("BOLSIG+"¹²) with appropriate electron energy-dependent cross sections for a range of reduced electric fields (E/N). The electron properties and the electron mean energies are determined as a function of E/N by the Boltzmann solver. These results are then used to tabulate the properties as a function of the electron mean energy (temperature) for use in the plasma discharge simulations. The ion transport properties are derived from experimental mobility data¹³ based on which the collision frequency $\bar{\nu}_i$ can be determined. Hard-sphere cross sections $\bar{\sigma}_{kb}$ based on the Lennard-Jones interaction potentials¹⁴ are used to determine the neutral transport properties using $\bar{\nu}_k = n_{k_b} \bar{g}_{kb} \bar{\sigma}_{kb}$, where \bar{g}_{kb} is the relative thermal speed of species k .

iii. Boundary Conditions

For the electron continuity equation, the electron flux at solid walls is specified using a kinetic Maxwellian flux conditions for consumption of electrons at the walls with a return flux of secondary electrons from the walls, i.e.

$$\bar{\Gamma}_e \cdot \hat{n} = \frac{1}{4} n_e \left(\frac{8k_B T_e}{\pi m_e} \right)^{1/2} - \gamma \bar{\Gamma}_{Ar^+} \cdot \hat{n}, \quad (7)$$

where, \hat{n} is the unit normal vector pointed toward the wall. The solid walls include the electrode and dielectric surfaces. The first term in Eq. (7) is the Maxwellian flux of electrons to the surface and the second term is the secondary electron emission flux from the surface. In this study, we assume that the secondary emission coefficient, γ , includes contributions from ion impact, fast atoms, metastable atoms, dimmers, and ultraviolet photons.

For the ions continuity and ions momentum equations, the flux of positive ions is set to 0 for all solid boundaries for which the electric field points away from the wall ($\vec{E} \cdot \hat{n} < 0$). If the electric field points towards the wall ($\vec{E} \cdot \hat{n} > 0$), the ion flux is extrapolated from the interior by imposing a zero gradient of the ion flux at the boundary.

The Maxwellian flux condition is imposed for the neutral species, given by

$$\bar{\Gamma}_n \cdot \hat{n} = \frac{1}{4} n_n \left(\frac{8k_B T_g}{\pi m_n} \right)^{1/2}. \quad (8)$$

For the electron energy equation, the following energy flux is imposed at solid walls,

$$Q_e^W = \frac{5}{2} k_B T_e \Gamma_e^W, \quad (9)$$

where, Γ_e^W is the electron wall number flux.

The potential on dielectric surfaces is determined using Gauss' law for the dielectric-gas interface boundary condition which depends on the total accumulated surface charge density at the surface.⁹ The equation for evolution of the net surface charge density, ρ_s , is given by,

$$\frac{\partial \rho_s}{\partial t} = \sum_{k=1}^{K_g} e Z_k \bar{\Gamma}_k \cdot \hat{n}. \quad (10)$$

iv. Plasma Chemistry and Surface Processes

A pure argon plasma gas chemistry is used which comprises six species: electrons (e), atomic argon ions (Ar^+), molecular argon ions (Ar_2^+), electronically excited atoms (Ar^*), electronically excited molecules (Ar_2^*), and the background argon atoms (Ar). Dimer species are included because of the relatively high pressures in the upstream section of the micronozzle (~ 100 Torr). The list of reactions considered in the study is given in Table I and comprises electron impact ionization and excitation reactions, Penning ionization reactions, three-body reactions for dimer excited species and ion formation, quenching and de-excitation reactions. As in the case of electron transport properties, the electron impact reaction rates are determined apriori by solving the zero-dimensional electron Boltzmann equation ("BOLSIG+"¹²) with appropriate electron energy-dependent reaction cross sections. These rates are tabulated as a function of the electron temperature using the same procedure as for the electron transport properties.

At solid surfaces all excited species and charged species are assumed to get quenched with unity sticking coefficient. Upon quenching at surfaces, each dimer ion and excited species is assumed to return to plasma as a pair of ground state neutral Ar atoms, while the monomer species return as single Ar atoms.

IV. Flow Module

Conservation equations for the gas mass density, mass-averaged gas velocity, and the gas energy are solved using compressible Navier-Stokes equations in axisymmetric form. These equations can be written as

$$\frac{d\mathbf{U}}{dt} + \vec{\nabla} \cdot \vec{\mathbf{F}}_{\text{inviscid}} = \vec{\nabla} \cdot \vec{\mathbf{F}}_{\text{visc}} + \mathbf{S}, \quad (11)$$

where, \mathbf{U} represents the conservative variables $(\rho, \rho V_x, \rho V_r, \rho e_t)$ (ρ is the background density, V_x is the axial velocity, V_r is the radial velocity, and e_t is the total internal energy of the gas), $\vec{\mathbf{F}}_{\text{inviscid}}$ represents the inviscid flux terms, $\vec{\mathbf{F}}_{\text{visc}}$ represents the viscous flux terms, and \mathbf{S} represents the source terms.

The flow solution influences the plasma discharge through the pressure, temperature and velocity fields appearing in the plasma governing equations (Eqs. (1)-(5)). On the other hand, electrostatic forces and electrothermal heating act as external body forces and external heat source, respectively, in the Navier-Stokes equations. These source terms are defined as

$$\vec{f} = \sum_i m_i n_i (\vec{u}_i - \vec{V}) \vec{v}_{i,k_b} - e n_e \vec{E}. \quad (12)$$

for the electrostatic force, and

$$S_{\text{heat}} = -\alpha_J (e \sum_h Z_h \bar{\Gamma}_h \cdot \vec{\nabla} \phi) + \frac{3}{2} k_B n_e \frac{2m_e}{m_{k_b}} (T_e - T_g) \vec{v}_{e,k_b} - e \sum_{j=1}^{I_g} \Delta E_j^g r_j, \quad (13)$$

for the electrothermal heating, such that $\mathbf{S} = (0, f_x, f_r, S_{\text{heat}})^T$. The first term on the RHS of Eq. (13) represents the effective ion Joule heating, taken here to be a fraction α_J ($0 < \alpha_J < 1$) of the local ion

Joule heating ($\bar{J}_{\text{ion}} \cdot \bar{E}$, where \bar{J}_{ion} is the total ion current density and \bar{E} is the local electric field). This fraction is < 1 for cases where the ion mean free path is comparable or larger than the characteristic length scale for the plasma, which results in incomplete conversion of the local kinetic energy gained by the ions in the electric field to ion/heavy species thermal energy. For microdischarge conditions, we use a fixed value of $\alpha_J = 0.25$ as suggested in Ref. 15. The Joule heating terms appearing in the electron energy equation (Eq. (3)) and in Eq. (13) are evaluated using a species flux reconstruction approach.¹⁶

V. Numerical Approach

Both the plasma governing equation and the compressible flow Navier-Stokes equations are spatially discretized using a cell-centered finite volume approach on an unstructured mesh with mixed mesh cell types. A steady state solution is sought in all cases. Both the plasma and flow governing equations are solved as transient problems with time-stepping of the solution to a steady state. The plasma governing equations are solved using an implicit time-discretization approach with local linearization of the governing equations at each time step. For the flow governing equations, the inviscid flux terms are evaluated with the Advection Upstream Splitting Methods (AUSM)¹⁷ and the viscous flux terms are evaluated using the Haselbacher approach.¹⁸ The flow equations are also solved using implicit time-discretization, with a dual-time stepping approach to iteratively solve for the solution at each time step. The viscous terms in the flow equations require computation of the solution variable gradients at cell centers. We use a Green-Gauss method to reconstruct these gradients based on cell-centered values of these variables. Finally, the compressible flow can develop shock discontinuities. The Venkatakrishnan¹⁹ flux limiter approach is used to stabilize and produce monotone solutions in the presence of such discontinuities.

VI. Physical Operating Conditions

Figure 1 shows the geometry of the MPT used for the simulations. The geometry consists of an axisymmetric constant area “pipe” section of 500 μm length, followed by a diverging section that is 200 μm in length, which is terminated by a 150 μm long constant area section. The radius of the upstream constant area pipe section is 50 μm , and the exit section is 150 μm in radius. The ring shaped electrodes have an axial thickness of 150 μm , while the dielectric layer has an axial thickness of 550 μm . The mesh consists of about 3600 cells, which includes a combination of triangles and quadrilaterals.

The flow direction is from left to right in Fig. 1. The flow enters the constant area pipe section on the left and exits the domain along the curved (arc-shaped) boundary on the right. Four boundary sections are not modeled as solid walls for the gas discharge governing equations. Zero-flux boundary conditions are imposed at the boundary section formed by the symmetry axis. For numerical stability reasons, zero-flux boundary conditions are also used for the gas discharge governing equations at the inlet and outer cathode surface boundaries. These boundaries are sufficiently away from the main discharge region and do not influence the results. The farfield boundary on the right side of the computational domain is modeled as an “outflow” boundary, where the plasma variables (species number densities and electron energy density) are convected away by the gas flow, while zero-flux boundary conditions are imposed for the Poisson’s equation. The value of the plasma variable from the adjacent interior cell is used to interpolate the flux at this farfield boundary. The power input is provided by applying a fixed positive DC voltage at the anode (without ballast resistance), while the cathode is grounded. For the base case, the secondary electron emission coefficient is set at a value of 0.03, corresponding to a nickel surface interacting with an argon plasma²².

The inlet total (stagnation) pressure is 100 Torr (for the base case), and a small but non-zero outlet pressure (0.05 Torr) is required to stabilize the numerical scheme in the “vacuum” part of the domain. The inlet gas static temperature is fixed at 300 K. The solid wall temperatures are fixed at 300 K. The inlet flow velocity is computed self-consistently using the inlet flow total conditions, the inlet static

pressure extrapolated from the interior of the domain and isentropic expansion relations. No-slip boundary conditions are applied at solid walls for the momentum equation. The Knudsen numbers for the flow are sufficiently low over much of the MPT device length (about 0.01 at the inlet to about 0.08 at the exit plane) that slip-flow and wall-temperature jump boundary condition is not necessary. This has been verified by running simulations with the appropriate jump boundary conditions.

VII. Results and Discussion

A. Base Case

Table II lists discharge conditions for which results are presented. For the base case, the discharge voltage is set at a value of 750 V, and the computed discharge current is 0.87 mA. The total stagnation pressure (100 Torr) and static temperature (300 K) imposed at the inlet determines inlet velocity which is computed at about 100 m/s corresponding to a flow rate of 5.2 sccm. Plasma properties at steady state are shown in Fig. 2 for the base case. The space charge density is high enough that the bulk plasma extends well into the diverging part of the micronozzle creating a hollow-cathode-like annular cathode sheath. Under these operating conditions, the cathode sheath is about 100- μm thick (see Fig. 2(a)), occupying a significant fraction of the total discharge volume. In the cathode fall, the potential drops by nearly 750 V over $\sim 100\ \mu\text{m}$ producing a characteristic field strength of $\sim 75\ \text{kV cm}^{-1}$ and a reduced electric field (electric field / gas number density) of $\sim 10^5\ \text{Td}$ (Townsend). Electron density contours are presented in Fig. 2(b) and show two local maxima. The first peak is inside the constant area pipe section ($\sim 7 \times 10^{19}\ \text{\#/m}^3$), and the second peak is in the diverging section of the nozzle ($\sim 3 \times 10^{20}\ \text{\#/m}^3$). The well-defined cathode sheath structure observed in Fig. 2(a) is apparent in the density contours with an abrupt drop in the electron densities in the diverging micronozzle section. The MPT discharge clearly operates in the glow discharge mode rather than the Townsend/predischARGE mode. The electron temperature contour is shown in Fig. 2 (c). The electron temperature is only shown in regions of the discharge where the electron number density is greater than $3 \times 10^{17}\ \text{\#/m}^3$, i.e. 10^{-3} of the peak value of the electron number density. The electron energy content is negligible in the rest of the domain, although the electron temperatures can increase exponentially in these regions of vanishingly small electron densities owing to a numerical artifact of the fluid model. The electron temperature remains nearly uniform ($\approx 2\ \text{eV}$) in the bulk plasma over most of the constant area pipe section, and gradually increases in the diverging section of the devices to temperatures around 3 eV at the cathode sheath edge.

The generation rate of electrons in the discharge through gas-phase reactions is shown in Fig. 2(d). Significant generation of electrons is observed over the entire micronozzle with maximum generation observed in the diverging section. This location corresponds to a relatively higher electron temperature ($\approx 3\ \text{eV}$) and reasonably high background densities in the expanding gas flow. The argon monomer ion (Ar^+) and dimer ion (Ar_2^+) number densities are shown in Figs. 2(e) and 2(f), respectively. Atomic argon ions constitute the dominant ion species in the microdischarge. High background densities favor the three-body reaction G_{12} (see Table I) that forms dimer species. Therefore, most dimer ions are located in the constant area pipe section, where the pressure is relatively high. The dielectric surfaces support a net negative charge owing to electron trapping which in turn supports a positive sheath over the entire dielectric length between the anode and the cathode. This is apparent from the excess of positive ions compared to electrons, just above the dielectric surfaces. The net negative charge at the dielectric enforces the electron wall flux to equal the total positive ion wall flux (at steady state), so no net current is drawn through the dielectric surfaces.

The Ar^+ ion number flux, computed using the ion momentum equation (Eq. (5)) is shown in Fig. 3. Most of the ions are generated in a localized region close to the axis in the diverging portion of the device and subsequently drift and diffuse away from this region. Most of the ions eventually drift towards the cathode and the dielectric surface in the vicinity of the cathode, where they are quenched. A negligibly

small fraction of the ions ($< 1\%$) leave the nozzle. Consequently, the electrostatic ion thrust contribution to the overall thrust produced by the MPT device is negligible.

The base case simulation was also run with the drift-diffusion approximation (Eq. (6)) used for ion transport, instead of the ion momentum equation (Eq. (5)). Comparison of the discharge results for the drift-diffusion ion simulation case (not shown) with the ion momentum case indicate that the results can be significantly different (e.g. the peak value of the monomer ion number densities differs by about 20% between the two cases), confirming the non-negligible role of the ion inertia in the MPT configuration.

The flow field solution for the base case is shown in Fig. 4. The major influence of the plasma on the flow field is through the heat addition that is shown in Fig. 4(a). We have confirmed through additional simulations that the electrostatic forcing source term in the flow momentum equation (Eq. (12)) has a negligible effect on the overall flow and discharge solutions. The thermal power deposition to gas (Eq. (13)) originates in large part from ion Joule heating in the cathode sheath. A peak in the gas heating is observed close to the MPT surface at the corner between the dielectric and the cathode where the electric fields are the highest. The gas temperature contours are shown in Fig. 4(b). The gas temperature contours show a peak value of about 950 K. The location of the peak temperature is slightly downstream and closer to the axis compared to the location of peak thermal power deposition. The localized power deposition in the immediate vicinity of the cathode surface leads to significant heat loss to the solid wall, indicating that thruster performance could be improved in the future by optimizing the design to minimize this loss.

The axial and radial velocity components, Mach number, and pressure fields are shown in Figs. 4(c) to 4(f). The axial velocity increases rapidly at the start of the diverging section owing to gas dynamic expansion, followed by a small decrease owing to compression waves launched from the straight cathode section. Subsequently, the axial velocity increases once it expands out the exit plane. Peak axial velocities greater than 550 m/s are seen outside the exit plane. The Mach number contours follow the trends in the axial velocity, with an increase at the start of the diverging section, followed by a decrease near the cathode section (owing to axial velocity decrease as well as an increase in the sound speed due to high temperatures), and a subsequent increase beyond the exit plane. The radial velocity profiles reflect the mass continuity requirements for the gas expansion process. The pressure profile shows a gradual, almost linear Poiseuille, pressure drop in the straight pipe section of the micronozzle, followed by a rapid decrease in the diverging section and out the exit plane. We must note that no sharp shock discontinuities are observed in the gas flow solution, owing mainly to the very low Reynolds number viscous dominated nature of the flow, despite the high Mach numbers. For these base case operating conditions, the computed thrust is 100 μN (compared to 67 μN for the cold gas micronozzle), which corresponds to a specific impulse of 74 s. The electrostatic component of thrust (owing to ion momentum leaving the exit plane) is found to be negligible and the thrust is almost entirely due to neutral momentum transport out the exit plane.

Figure 5 shows a schematic of the energy flow pathways in the MPT. The electrical power input (the discharge current times the discharge voltage) for the base case is 650 mW. Of this, most of the power (about 550 mW) is attributed to ion Joule heating integrated over the entire domain ($\int_V \vec{J}_{ion} \cdot \vec{E} dV$), while the electron Joule heating ($\int_V \vec{J}_e \cdot \vec{E} dV$) is about 45 mW. The mismatch between the input electrical power and the integrated Joule heating in the domain (ion and electron) is attributed to numerical discretization error. According to our model a large fraction of the ion Joule heating is lost to the wall while the remaining is thermalized to provide a source term to the gas energy equation. This fraction is set by the parameter α_J which equals 0.25 in these simulations. Consequently, 75% of the intrinsic ion Joule heating is lost directly to the wall surfaces. A small fraction (less than 1%) of the power deposited in the heavy species thermal pool (gas energy) is lost through inelastic collisions, while the rest is lost at solid walls and at the outflow section. The rate of energy transfer from the electron thermal pool to the heavy species (gas) thermal pool through inelastic collisions amounts to a small fraction of the electron Joule heating (less than 1%). A significant amount of power (35 mW or $\sim 80\%$ of the electron Joule

heating) is lost through inelastic collisions, while the rest of the power deposited in the electron thermal pool is lost through transport at solid walls and at the outflow section

VIII. Effect of Power Input

Figure 6 shows the effects of power input on discharge characteristics. Results are presented for the base case (where the discharge voltage is fixed at 750 V) and for a case where the discharge voltage is fixed at 1000 V. For both cases, the inlet total pressure is 100 Torr and the flow rate is 5.2 sccm. The plasma is more intense (i.e. the ionized species number densities are higher) for higher power inputs. Electron and dominant ion Ar^+ number densities increase by a factor of ~ 2 as the power input is increased from 650 mW (base case) to 1800 mW.

Figure 7 shows the effect of power input on flow properties. Contours of the power deposition in the MPT are shown in Fig. 7(i). The net power deposition into neutral gas scales almost linearly with the power input as the ratio between these two quantities remains equal to about 20% for both cases. Gas temperatures contours are shown in Fig. 7(ii). A peak temperature of 1850 K is reached for the high power case (compared to 950 K for the base case). Importantly, these results show that changing the external power input is an effective method to control the level of gas heating in the discharge, which, in turn, affects the gas temperature and the thrust produced by the device. This constitutes a key feature of our proposed MPT concept. The computed thrust increases to a value of 128 μ N for the high power case, which corresponds to a specific impulse of 95 s.

IX. Effect of Pressure / Flow Rate

We now vary the inlet total (stagnation) pressure to 200 Torr (the base case inlet total pressure is 100 Torr). Other conditions such as the inlet static temperature (300 K) and the discharge voltage drop (750 V) are kept the same as the base case. The increase of the inlet total pressure causes an increase of flow rate through the micronozzle to a value of 13 sccm (compared to 5.2 sccm for the base case). Contours of the axial velocity are shown in Fig. 8(i). Higher flow velocities and gas mass-densities (not shown) are observed throughout the nozzle for the high pressure case. The change in flow field has a profound effect on the microdischarge characteristics. The high velocities combined with decreased diffusive transport properties lead to a further downstream convection of the ionized species. The discharge also appears more constricted for the high pressure case with a slightly lower peak charge density for the high pressure case. The higher pressures decrease the plasma conductivity resulting in a decrease in the discharge current to 0.75 mA (compared to 0.87 mA for the base case). The resulting input power decreases for the high pressure case to about 560 mW (compared to 650 mW for the base case). The peak gas temperature also decreases compared to the base case (600 K compared to 950 K, not shown) owing to lower power deposition and also because of the increased heat capacity of the higher pressure gas. Case studies were also performed with a lower total inlet pressure of 60 Torr. For these conditions, the microdischarge could not be sustained for discharge voltages ranging from 750 V to 1000 V.

X. Sensitivity to Model Parameters

1. Cathode Temperature

Since a large fraction of the input power is lost to the walls, the cathode temperature can be expected to be significantly higher than the constant 300 K assumed in the above results. An accurate estimate of the cathode temperature would require solving an energy balance equation for the entire MPT device (including solid materials).

The effect of the cathode temperature on the MPT discharge parameters and performance is studied by comparing the base case solution to a case where the cathode temperature is fixed at 1000 K. All other conditions are kept the same as the base case. Figure 9(i) plots the gas temperature contours for the two

cases. The spatial distribution of gas temperature appears strongly dependent on the cathode temperature. For the case where the cathode temperature is fixed at 1000 K, the peak gas temperature reaches 1150 K (compared to 950 K for the base case) and the region of high gas temperatures occupies a larger fraction of the MPT volume than for the base case. Increasing the cathode temperature reduces the temperature gradients at the cathode surface, thereby decreasing the net thermal loss.

The axial velocity contours are shown for the two cases in Fig. 9(ii). As the cathode temperature is increased, the reduced heat losses allow for an increased expansion of the gas in the diverging section of the micronozzle. The computed thrust therefore increases from a value of 100 μN for the base case to a value of 112 μN for the 1000 K cathode temperature case. It should be noted that, for this higher cathode temperature case, the power input has decreased to a value of 540 mW, compared to 650 mW for the base case. The higher gas temperatures (and therefore lower background *Ar* densities) result in a decrease in ionization. The lower power/current can be attributed to the lower charge densities and hence to the lower plasma conductivity.

2. Fraction of Ion Joule Energy Thermalized with the Gas

For high-pressure microdischarges and conventional discharges at very low pressures, a large fraction of the kinetic energy of the ions is deposited directly onto discharge bounding surfaces, particularly the cathode. This phenomenon has been simulated by Revel *et al.*²¹ using a particle-in-cell Monte-Carlo approach for a one-dimensional argon discharge. For current densities of $\sim 20 \text{ A/m}^2$, an interelectrode distance of 1.5 cm, and a background pressure of 1 Torr, they observe that $\sim 25\%$ of the ion Joule energy is converted to gas thermal energy, with the remainder being transferred directly to the cathode. Boeuf *et al.*¹⁵ used a nominal fixed value of $\alpha_J = 0.25$ for simulation studies of a 100 Torr xenon micro-hollow cathode discharge, which is the same value used in our study.

The sensitivity of our model results to this parameter is determined by varying α_J to 0.5. The power deposition and gas temperatures contours are shown in Fig. 10 for both cases. Since most of the thermal (gas) power deposition in the MPT is attributed to ion Joule heating, the thermal power deposition increases significantly from a value of 140 mW for the base case to 260 mW when $\alpha_J = 0.5$. At the same time, the total input power to the MPT decreased to 540 mW (compared to 650 mW for the base case). As described in the previous section, the increase of the gas temperature (to a peak value of 1350 K) results in decreased neutral density, with a resulting decrease in ionization rate and hence the charge density. Consequently, the plasma conductivity decreases resulting in decreased current and total power deposition into the discharge. The increased fraction of power deposited into gas improves the efficiency of the device. The computed thrust increases to 116 μN (compared to 100 μN for the base case).

Our model assumes a constant value of α_J . In reality, this parameter will depend on the local background pressure. Indeed, as the mean free path of ions decreases with increasing pressure, ions will deposit a larger fraction of their kinetic energy to the background gas. In future studies we will explore more accurate strategies (e.g. hybrid models) to model this effect consistently.

3. Secondary Electron Emission Coefficient

The value of the secondary electron emission coefficient, γ , constitutes an important uncertain parameter of the plasma model. This coefficient is sensitive to surface conditions and its value can vary by several orders of magnitude depending on the surface material and the cleanliness of the surface. In the above simulation results, we chose a constant value of $\gamma = 0.03$ (corresponding to a nickel surface interacting with an argon plasma).²² The sensitivity of our results to this parameter is analyzed by comparing our base case to a case with $\gamma = 0.01$. The discharge current is significantly reduced for the model with the lower secondary electron coefficient (to a value of 0.33 mA). Lower γ results in fewer electrons released from the surface through Auger processes per ion impact, which in turn results in a much weaker discharge. This behavior is characteristic of all gamma-mode discharges such as the direct-current microdischarge presented in this study.²³⁻²⁴

Figure 11 shows the ion number density and gas temperature contours obtained with the two models for a discharge voltage of 750 V. While the peak ion number density has about the same value ($\sim 3 \times 10^{20} \text{ \#/m}^3$) for both cases, the discharge activity appears more constricted for the lower γ case. Since the ion Joule heating scales with the current, a significant decrease in power deposition into the neutral gas is observed (not shown). This results in a decrease of the gas temperature (shown in Fig. 11(ii)) and a decrease in the computed thrust to a value of 87 μN , compared to 100 μN for the base case.

XI. Conclusion

Microdischarge and flow interaction phenomena for micropropulsion applications have been studied using a detailed self-consistent computational model. The model consists of a plasma module coupled to a flow module and is solved on a hybrid unstructured mesh framework. The plasma module provides a self-consistent, multi-species, multi-temperature description of the microdischarge phenomena while the flow module provides a description of the low Reynolds number compressible flow through the micropropulsion system.

The Micro Plasma Thruster (MPT) concept consists of a direct-current microdischarge in a geometry comprising a constant area flow section followed by a diverging exit nozzle. The coupled plasma-flow simulations showed that the electrostatic component of thrust is negligible for our current MPT configuration. Electrothermal heating is due primarily to the ion Joule heating occurring near the cathode surfaces. A large part of the input power is therefore deposited into the walls rather than going to neutral gas heating. Future work must explore strategies that will allow for power deposition away from the wall, near the centerline. For example, radio-frequency operation of the microdischarge may help reduce the thermal load on the microdischarge, and increase the direct power deposition into the neutral gas.

For a discharge voltage of 750 V, a power input of 650 mW, and an argon mass flow rate of 5.2 sccm, the specific impulse of the device is 74 s, a factor of ~ 1.5 increase compared to the cold gas micronozzle. For these conditions, charged species densities on the order of $5 \times 10^{20} \text{ m}^{-3}$ and peak gas temperatures of $\sim 1000 \text{ K}$ are predicted. The microdischarge remains mostly confined inside the micronozzle and operates in an abnormal regime. Additional simulation studies on the MPT indicate that the power input has a strong influence on overall discharge properties. The net power deposition into the neutral gas scales with the power input, providing a method of controlling the gas temperature and the thrust level of the MPT. This feature constitutes an important advantage over traditional cold gas thrusters.

The sensitivity of above results to important uncertain parameters of the model has been studied. These parameters are the cathode temperature, the fraction of ion Joule heating that is locally converted to gas thermal energy, and the secondary electron coefficient. A higher cathode temperature is found to reduce the heat losses at solid walls and is beneficial for the thruster performance, though there is obviously an upper limit to avoid damage to the cathode. The cathode temperature could be evaluated by solving the solid thermal conduction equation in the dielectric and electrode material to quantify the overall thermal field in the MPT device. The thermal loads from the plasma at the wall surfaces will drive heat transfer into the device structure potentially resulting in "hot spots" that can be investigated through the simulations. These coupled multi-physics simulation results would in turn provide an informed approach to the better designs of the MPT device from a thermal viewpoint. Finally, the voltage-current characteristics of the device is found to be very sensitive to the value of the secondary electron coefficient used in the model. Future studies of the MPT should include a calibration of these uncertain parameters and a validation of the model with experimental results.

References

- ¹Micci, M. M., and Ketsdever, A. D., *Micropropulsion for Small Spacecraft*, Progress in Astronautics and Aeronautics, AIAA, Reston, VA, 2000.
- ²Sweeting, M. N., "Space at Surrey: micro-mini-satellites for affordable access to space," *Air and Space Europe*, Vol. 2, 2000, pp. 38-52.

- ³Brown, C. D., *Spacecraft Propulsion*, American Institute of Aeronautics and Astronautics, Washington, DC, 1996.
- ⁴Xie, C., "Characteristics of micronozzle gas flows," *Physics of Fluids*, Vol. 19, 2007, 037102.
- ⁵Alexeenko, A. A., Levin, D. A., Gimelshein, S. F., Collins, R. J., and Reed, B. D., "Numerical modeling of axisymmetric and three-dimensional flows in microelectromechanical systems nozzles," *AIAA Journal*, Vol. 40, 2002, pp. 897-904.
- ⁶Williams, K. L., Eriksson, A. B., Thorslund, R., Köhler, J., Boman, M., and Stenmark, L., "Numerical modeling of axisymmetric and three-dimensional flows in microelectromechanical systems nozzles," *Journal of Micromechanics and Microengineering*, Vol. 16, 2006, pp. 1154-1161.
- ⁷KC, U., Bingaman, J., Varghese, P. L., and Raja, L. L., "Studies of a direct-current microdischarge based miniaturized plasma thruster," *Proceedings of the 2nd European Conference for Aerospace Sciences*, Brussels, Belgium, 2007.
- ⁸Coxhill, I. G., Gibbon, D., "A Xenon Resistojet Propulsion System for Microsatellites," *Proceedings of the 41st AIAA/ASME/SAE/ASEE Joint Propulsion Conference and Exhibit*, AIAA paper 2005-4260, Tucson, AZ, 2005.
- ⁹Kothnur, P. S. and Raja, L. L., "Simulation of direct-current microdischarges for application in electro-thermal class of small satellite propulsion devices," *Contributions to Plasma Physics*, Vol. 47, 2007, pp. 9-18.
- ¹⁰Arakoni, R. A., Ewing, J. J., and Kushner, M. J., "Microdischarges for use as microthrusters: modeling and scaling," *Journal of Physics D: Applied Physics*, Vol. 41, 2008, pp. 1-12.
- ¹¹Mahadevan, S. and Raja, L. L., "Simulations of direct-current air surface plasma discharges in supersonic flow," *Proceedings of the 47th AIAA Aerospace Sciences Meeting and Exhibit*, AIAA paper 2009-1192, Orlando, FL, 2009.
- ¹²Hagelaar, G. J. M. and Pitchford, L. C., "Solving the Boltzmann equation to obtain electron transport coefficients and rate coefficients for fluid models," *Plasma Sources Science and Technology*, Vol. 14, 2005, pp. 722-733.
- ¹³Ellis, H. W., Pai, R. Y., McDaniel, E.W., Mason, E.A. and Vielhand, L.A., "Transport properties of gaseous ions over a wide energy range," *Atomic Data & Nuclear Data Tables*, Vol. 17, 1976, pp. 177-210.
- ¹⁴Kee, R., Dixon-Lewis, G., Warnatz, J., Coltrin, M., and Miller, J., "A Fortran computer code package for the evaluation of gas-phase multicomponent transport properties," Technical report, Sandia Report SAND86-8246, 1995.
- ¹⁵Boeuf, J. P., Pitchford, L. C., and Schoenbach, K. H., "Predicted properties of microhollow cathode discharges in xenon," *Applied Physics Letters*, Vol. 86, 2005, p. 071501.
- ¹⁶Deconinck, T., Mahadevan, S., and Raja, L. L., "Discretization of the Joule heating term in plasma discharge fluid models using unstructured meshes," *Journal of Computational Physics*, in review.
- ¹⁷Liou, M.-S. and Steffen, C. J., "A new flux-splitting scheme," *Journal of Computational Physics*, Vol. 107, 1993, pp. 23-39.
- ¹⁸Haselbacher, A. and Blazek, J., "Accurate and Efficient Discretizations of Navier-Stokes Equations on Mixed Grids," *AIAA Journal*, Vol. 38, 2000, pp. 2094-2102.
- ¹⁹Venkatakrishnan, V., "Convergence to steady state solutions of the Euler equations on unstructured grids with limiters," *Journal of Computational Physics*, Vol. 118, 1995, pp. 120-130.
- ²⁰Lay, B., Moss, R. S., Rauf, S., and Kushner, M. J., "Breakdown processes in metal halide lamps," *Plasma Sources Science and Technology*, Vol. 12, 2003, pp. 8-21.
- ²¹Revel, I., Pitchford, L. C., and Boeuf J.-P., "Calculated gas temperature profiles in argon glow discharges," *Journal of Applied Physics*, Vol. 88, 2000, pp. 2234-2239.
- ²²Lieberman, M. A., and Lichtenberg, A. J., *Principles of Plasma Discharges and Materials Processing*, John Wiley & Sons, New York, 1994.
- ²³Kushner, M. J., "Modelling of microdischarge devices: plasma and gas dynamics," *Journal of Physics D: Applied Physics*, Vol. 38, 2005, pp. 1633-1643.

²⁴Wang, Q., Economou, D. J., and Donnelly, V. M., "Simulation of a direct current microplasma discharge in helium at atmospheric pressure," *Journal of Applied Physics*, Vol. 100, 2006, p. 023301.

#	Reactions	Reaction rate ^a	Ref.
G1	$e + \text{Ar} \rightarrow e + \text{Ar}$	b	12
G2	$e + \text{Ar} \rightarrow e + \text{Ar}^*$	b	12
G3	$e + \text{Ar} \rightarrow 2e + \text{Ar}^+$	b	12
G4	$e + \text{Ar}^* \rightarrow 2e + \text{Ar}^+$	b	12
G5	$e + \text{Ar}^* \rightarrow e + \text{Ar}$	b	12
G6	$e + \text{Ar}^+ \rightarrow \text{Ar}^*$	$4.0 \times 10^{-13} T_e^{-0.5}$	20
G7	$2e + \text{Ar}^+ \rightarrow \text{Ar}^* + e$	$5.0 \times 10^{-27} T_e^{-4.7} \text{ cm}^6 \text{ s}^{-1}$	20
G8	$e + \text{Ar}_2^+ \rightarrow \text{Ar}^* + \text{Ar}$	$5.38 \times 10^{-8} T_e^{-0.66}$	20
G9	$2\text{Ar}^* \rightarrow \text{Ar}^+ + \text{Ar} + e$	5×10^{-10}	20
G10	$2\text{Ar}_2^* \rightarrow \text{Ar}_2^+ + 2\text{Ar} + e$	5×10^{-10}	20
G11	$\text{Ar}^* + 2\text{Ar} \rightarrow \text{Ar}_2^* + \text{Ar}$	$1.14 \times 10^{-32} \text{ cm}^6 \text{ s}^{-1}$	20
G12	$\text{Ar}^+ + 2\text{Ar} \rightarrow \text{Ar}_2^+ + \text{Ar}$	$2.5 \times 10^{-31} \text{ cm}^6 \text{ s}^{-1}$	20
G13	$\text{Ar}_2^* \rightarrow 2\text{Ar}$	$6.0 \times 10^7 \text{ s}^{-1}$	20
G14	$e + \text{Ar}_2^* \rightarrow 2e + \text{Ar}_2^+$	$9 \times 10^{-8} T_e^{0.7} \exp(-3.66/T_e)$	20
G15	$e + \text{Ar}_2^* \rightarrow e + 2\text{Ar}$	10^{-7}	20

^a Rate coefficients have units of $\text{cm}^3 \text{ s}^{-1}$, unless mentioned otherwise. Electron temperatures, T_e , are in eV.

^b Tabulated rate coefficient as a function of mean electron temperature was obtained by the Boltzmann equation solver "BOLSIG+".¹²

Table I. High-pressure argon plasma gas-phase chemistry used in this study.

Case	Inlet total pressure (Torr)	$P D$ (Torr cm)	Flow rate (sccm)	Voltage (V)	Current (mA)	Power (mW)
Base case	100	5.5	5.2	750	0.87	650
Larger power input	100	5.5	5.2	1000	1.8	1800
Larger pressure / flow rate	200	11.0	13	750	0.75	560
Larger cathode temperature	100	5.5	5.2	750	0.72	540
Larger α_J	100	5.5	5.2	750	0.72	540
Lower γ_{eff}	100	5.5	5.2	750	0.33	250

Table II. Operating conditions considered for this study. The characteristic discharge dimension D is taken to be the thickness of the dielectric layer located between the electrodes (550 μm) and the characteristic pressure is taken to be the inlet total pressure.

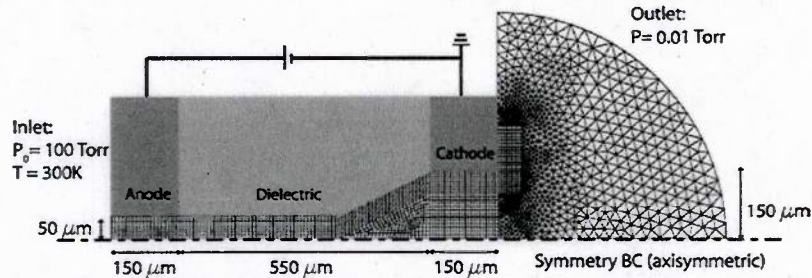


Figure 1. Schematic of the MPT device and computational mesh. The geometry is cylindrically symmetric.

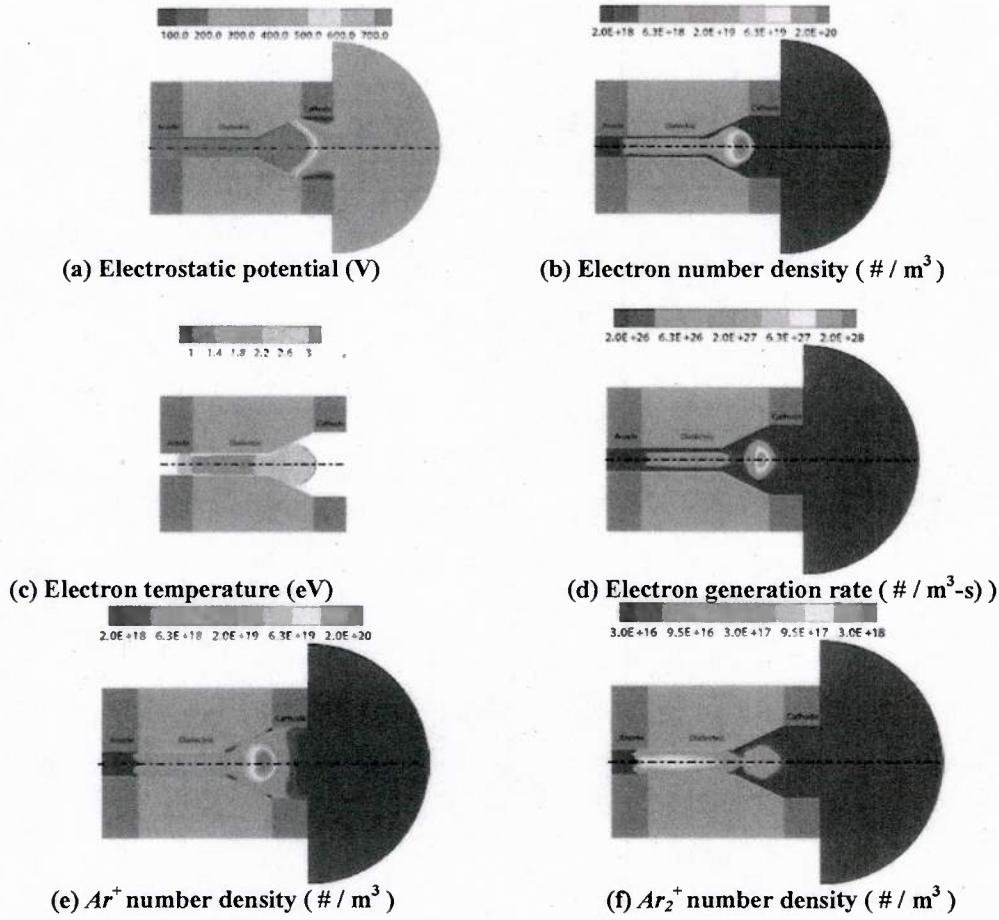


Figure 2. Plasma properties in the MPT. The inlet total pressure is 100 Torr (13.3 kPa) and the mass flow rate is 5.2 sccm. The applied potential difference between the electrodes is 750 V and the power input is 650 mW.

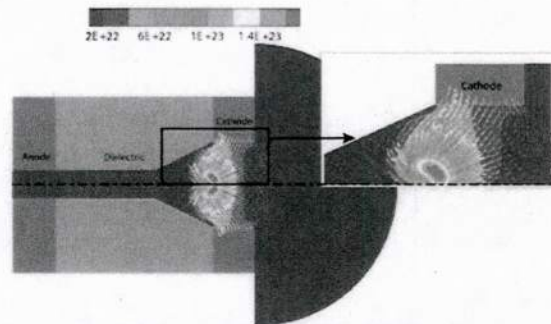


Figure 3. Monomer (Ar^+) ion number flux ($\# / \text{m}^2\text{-s}$) in the MPT. The contours indicate the magnitude of the ion number flux. The vectors indicate the direction of ion flux, which the length of arrows being proportional to the flux magnitude. The operating conditions correspond to the base case indicated in Fig. 2 caption.

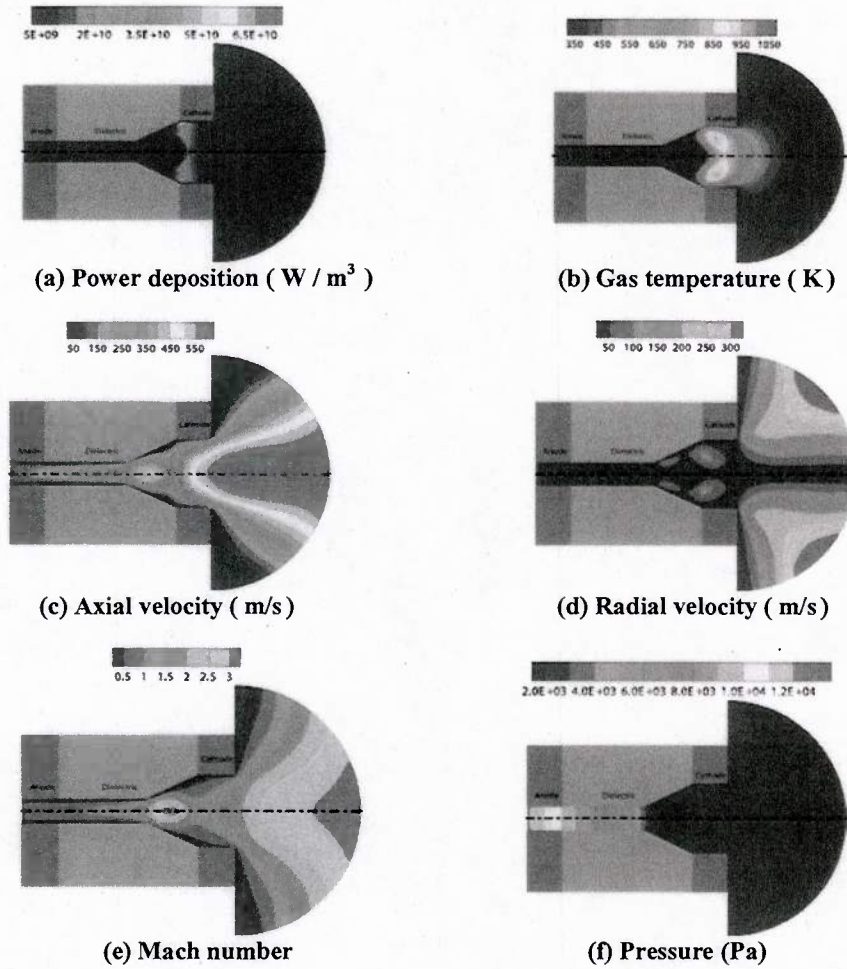


Figure 4. Flow properties in the MPT. The operating conditions are indicated in Fig. 2 caption.

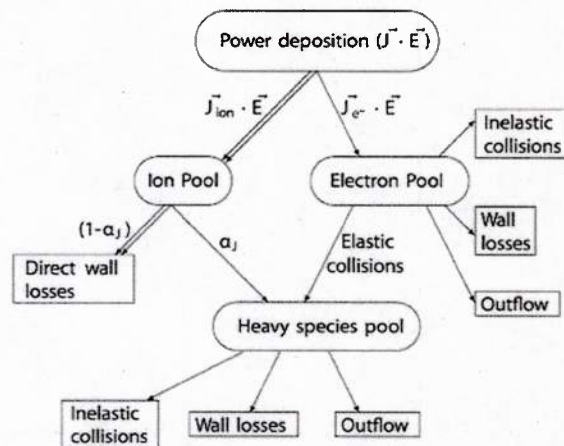
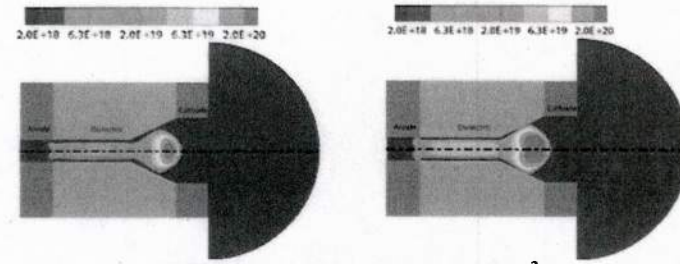
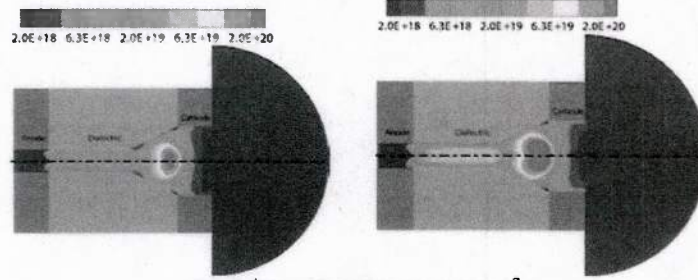


Figure 5. Energy flow pathways in the MPT.



(i) Electron number density ($\# / \text{m}^3$)

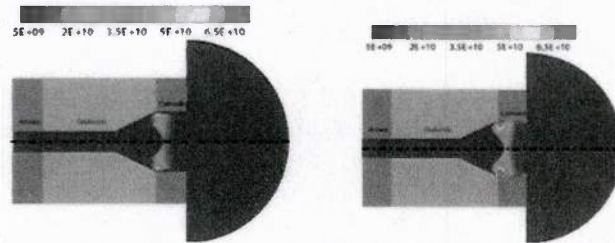


(ii) Ar^+ number density ($\# / \text{m}^3$)

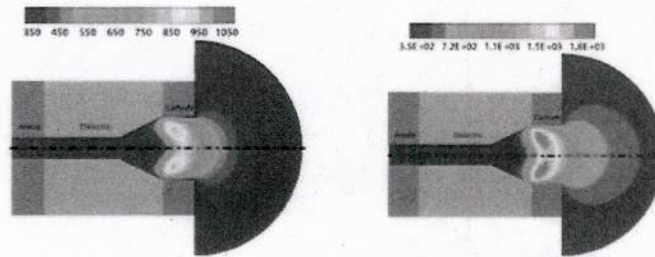
(a) Power input: 650 mW

(b) Power input: 1800 mW

Figure 6. Electron and dominant ion (Ar^+) number density contours for different values of the power input. The inlet total pressure is 13.3 kPa (100 Torr) and the flow rate is 5.2 sccm for both cases.



(i) Power deposition (W / m^3)



(ii) Gas temperature (K)

(a) Power input: 650 mW

(b) Power input: 1800 mW

Figure 7. Power deposition and gas temperature contours for different values of the power input. The inlet total pressure is 13.3 kPa (100 Torr) and the flow rate is 5.2 sccm for both cases.

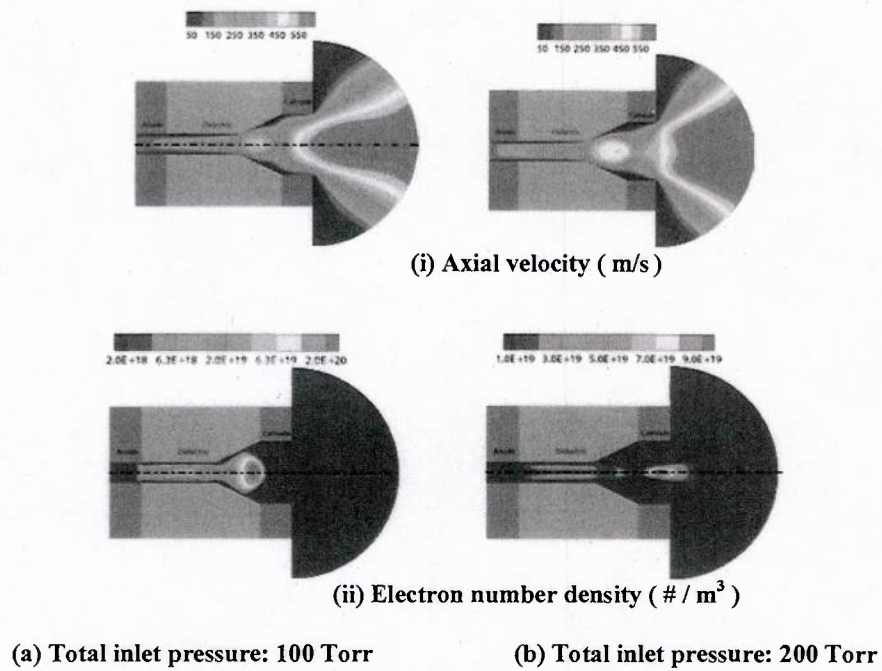


Figure 8. Axial velocity and electron number density contours for different values of the inlet total pressure / flow rate. Other conditions are same as the base case. The discharge voltage is fixed at 750 V for both cases.

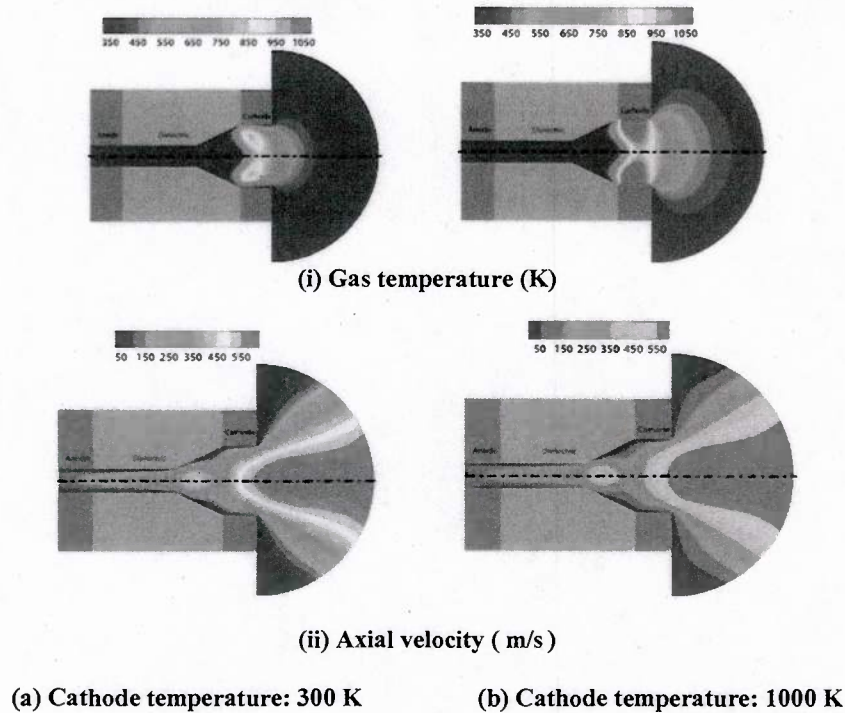


Figure 9. Gas temperature and axial velocity contours for different values of the imposed temperature at the cathode. The flow rate is 5.2 sccm and the applied potential difference between the electrodes is 750 V.

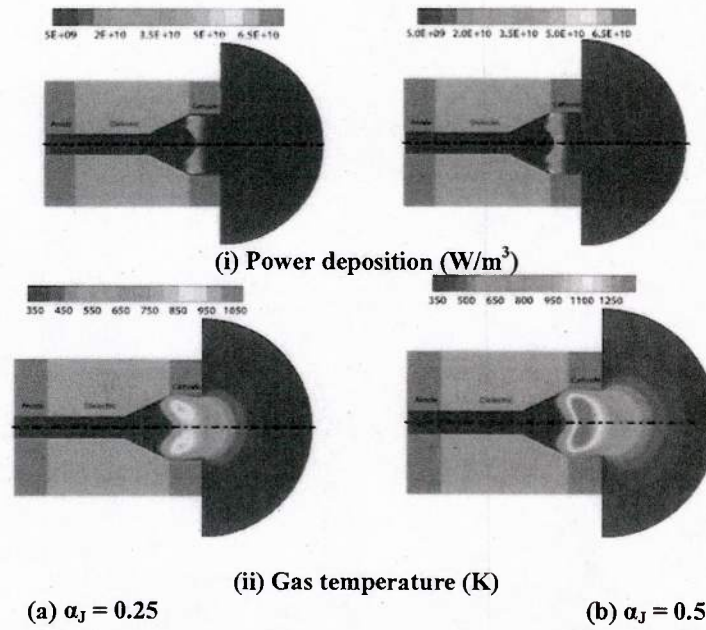


Figure 10. Power deposition and gas temperature contours for different fractions of ion Joule energy converted to gas thermal energy. The flow rate is 5.2 sccm and the applied potential difference between the electrodes is 750 V.

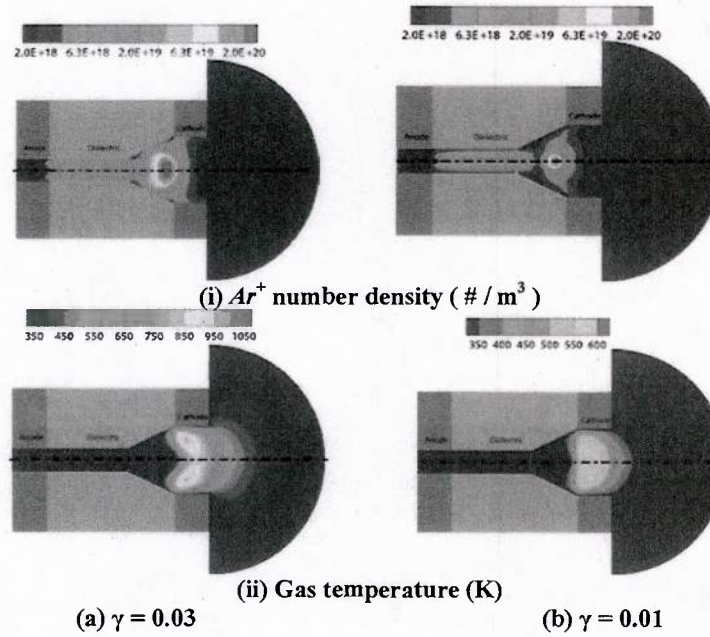


Figure 11. Dominant ion (Ar^+) number density and gas temperature contours for different values of the secondary electron emission coefficient. The flow rate is 5.2 sccm and the applied potential difference between the electrodes is 750 V.

Personnel supported:

Laxminarayan L. Raja – Associate Professor, Dept. of Aerospace Engr. and Engr. Mech.
Philip L. Varghese – Professor, Dept. of Aerospace Engr. and Engineering Mech.
Kc Utsav – Graduate Research Assistant (Ph.D)
Thomas Deconinck -- Graduate Research Assistant (Ph.D)

Publications:

Journal:

1. P. S. Kothnur and L. L. Raja, "Simulation of direct-current microdischarges for application in electro-thermal class of small satellite propulsion devices," *Contributions to Plasma Physics*, Vol. 27, No. 1-2, Feb. 2007, pp. 9-18.
2. T. Deconinck, S. Mahadevan and L. L. Raja*, "Simulation of a Direct-Current Microdischarge for the Micro Plasma Thrusters," *IEEE Transactions on Plasma Science*, Vol. 36, No. 4, Aug. 2008, pp. 1200-1201. (5th Triennial Special Issue on Images in Plasma Science).
3. T. Deconinck, S. Mahadevan, and L. L. Raja*, "Discretization of the Joule Heating Term for Plasma Discharge Fluid Models in Unstructured Meshes," *Journal of Computational Physics*, (in review).
4. T. Deconinck and L. L. Raja*, "Modeling of Mode Transition Behavior in Argon Microhollow Cathode Discharges," *Plasma Processes and Polymers*, (in print). (**Invited paper**)

Conference papers and talks:

1. U. KC, J. Bingaman, P. L. Varghese, and L. L. Raja, "Studies of a Direct Current Microdischarge Based Miniaturized Plasma Thruster", 2nd European Conference for Aerospace Sciences (EUCASS), Brussels, Belgium, July 1-6, 2007.
2. T. Deconinck, S. Mahadevan, and L. L. Raja, "Simulation studies of direct-current microdischarges for microelectric propulsion," 4th International Workshop on Microplasmas, Tainan, Taiwan, Oct. 29, 2007.
3. T. Deconinck, S. Mahadevan, and Laxminarayan Raja, "Simulation Studies of Direct-Current Microdischarges for Electric Propulsion," AIAA Paper 2009-1382, 47th AIAA Aerospace Sciences Meeting, Orlando, FL, 5-8 January 2009.